GABA Neurons in the Amygdala play a central Role in Urocortin-3–Mediated Stress Suppression of Reproduction

Author Information

Junru Yu[1,2,†], Saeed Farjami[3,4,5†] , Kateryna Nechyporenko[3,4,†], Xiao Feng Li[1], Hafsa Yaseen[1,6], Yanyan Lin[1], Jinbin Ye[1], Owen Hollings[1], Ross de Burgh[1], Baban Singh[1], Kevin T. O'Byrne[1,*], Krasimira Tsaneva-Atanasova[3,4,7,*], Margaritis Voliotis[3,4,*]

Affiliations

[1]Department of Women and Children's Health, School of Life Course and Population Sciences, King's College London, Guy's Campus, London SE1 1UL, UK, [2]Department of Rehabilitation Medicine, The First Affiliated Hospital of Wenzhou Medical University, Wenzhou, Zhejiang 325000, China, [3]Department of Mathematics and Statistics, Stocker Road, Exeter EX4 4PY, UK, [4]Living Systems Institute, Exeter EX4 4QD, UK, [5]The Pirbright Institute, Ash Road, Pirbright, Surrey GU24 0NF, UK, [6]Biological Sciences, University of Missouri, Columbia, MO 65211-7400 and [7]EPSRC Hub for Quantitative Modelling in Healthcare, University of Exeter, Stocker Road, Exeter EX4 4PY, UK

Correspondence to: Krasimira Tsaneva-Atanasova (k.tsaneva-atanasova@exeter.ac.uk), Kevin T. O'Byrne (kevin.o'byrne@kcl.ac.uk), Margaritis Voliotis (m.voliotis@exeter.ac.uk).

Abstract

Stress can disrupt menstrual cycles, cause infertility, and lead to other reproductive disorders. The posterodorsal medial amygdala (MePD) processes stress signals and regulates the gonadotropin-releasing hormone (GnRH) pulse generator through GABAergic inhibitory projections to the hypothalamus. However, how stress is processed in the MePD - especially involving its dense GABA and Urocortin-3 (UCN3) neurons - remains poorly understood.

In this study, we combine *in vivo* GRadient-INdex (GRIN) lens mini-endoscopic calcium imaging (to track neuronal activity), optogenetics, clustering analysis, and computational modeling to investigate the MePD circuitry. Our findings reveal two anti-correlated GABA subpopulations in the MePD that dictate responses to both UCN3 neuron stimulation and restraint stress. Our computational modeling suggests that mutual inhibition between these GABA groups drives the anti-correlated activity and predicts how these interactions shape downstream responses to stimulation of GABA and UCN3 neurons.

We test these predictions using optogenetics and confirm that GABA neurons are critical for the transmission of UCN3 signals to regulate luteinizing hormone (LH) pulse frequency. Our study is the first to show how GABA neurons in the amygdala mediate stress effects on reproductive health, uncovering key neural mechanisms linking emotional and reproductive functions.

Introduction

Successful reproduction requires normal function of a neural oscillator, the gonadotropin-releasing hormone (GnRH) pulse generator, that drives the pulsatile release of gonadotropic hormones, luteinizing hormone (LH) and follicle stimulating hormone (FSH) to control ovulation and spermatogenesis. This oscillator comprises Kisspeptin neurons co-expressing Neurokinin-B (NKB) and Dynorphin A (acronym KNDy) in the hypothalamic arcuate nucleus (ARC). The KNDy neural network not only provides the essential episodic stimulatory kisspeptin signal to the GnRH neurons, but receives diverse afferent inputs and hence is a hub for integrating various internal and external cues that regulate reproductive function[1,2]. Despite the marked heterogeneity of the myriad stressors, including acute versus chronic experimental stress paradigms, the common denominator is suppression of GnRH pulse generator frequency, which is associated with stress-related reproductive disorders and infertility[3–8].

The amygdala, a part of the limbic brain typically associated with emotions and anxiety, has strong projections to the KNDy system[1,2]. The medial amygdala, and more specifically its posterodorsal subnucleus (MePD), has been shown to be a robust upstream regulator of GnRH pulse generator frequency[9–11], pubertal timing[12,13], sociosexual behavior[14,15], anxiety[14] and psychological stress-induced suppression of pulsatile LH secretion[16,17].

In the MePD, the majority of neurons are GABAergic, accounting for a substantial portion of its projections, many of which target important hypothalamic centers involved in reproduction[18–20], including the KNDy neurons and optogenetic stimulation of the latter suppresses LH pulsatility[17]. Moreover, chemogenetic inhibition of GABA neurons in the MePD can reverse the inhibitory effect of psychogenic stress on LH pulsatility[17], suggesting an involvement of GABA signaling in the stress-induced suppression of pulsatile LH secretion. Although the precise way in which the MePD GABA neurons influence LH pulsatility is not fully understood, it has been suggested that they interact with the stress neuropeptide urocortin-3 (UCN3) neurons to modulate or reinforce stress-induced suppression of LH pulse frequency[16].

65 UCN3, part of the corticotropin-releasing factor (CRF) superfamily and selective for CRF type 2
66 receptors (CRFR2)[21], is highly expressed in the MePD[16,22]. Furthermore, UCN3 neurons in the MePD
67 mediate psychosocial stress-induced suppression of the GnRH pulse generator and corticosterone
68 secretion, thus playing a central role in the interaction between the reproductive and stress axes[16,23].
69 Previously we have shown that intra-MePD GABA antagonism can reverse UCN3-induced LH pulse
70 suppression[23], suggesting that GABA acts downstream of UCN3 signaling within the MePD. However,
71 the local neural circuitry within the MePD mediating stress related information to the GnRH pulse
72 generator remains to be established.

73 Here, we employed GRadient INdex (GRIN) lens mini-endoscopy to monitor and compare the calcium
74 activity of GABA neurons at single-cell resolution under acute psychological stress or optogenetic
75 stimulation of UCN3 neurons. Clustering analysis of the observed calcium transients uncovered two
76 distinct GABA subpopulations exhibiting anti-correlated activity. To explore the functional role of these
77 two subpopulations and unpick the mechanisms driving their anti-correlated activity, we build upon
78 our previously developed MePD circuitry mathematical modeling framework[11]. Our modeling reveals
79 that mutual inhibitory interactions between the GABA populations are sufficient to drive anti-correlated
80 activity and predicts a complementary inhibitory effect of GABA and UCN3 signaling on the frequency
81 of the GnRH pulse generator, which we tested by applying Cre/Flp recombinase intersectional
82 strategies to selectively target and manipulate heterogeneous MePD neuronal populations[17]. Hence,
83 by uncovering precise interactions between distinct subpopulations of MePD GABA neurons and
84 UCN3 neurons in transmitting stress signals to the GnRH pulse generator, we provide critical and
85 previously unknown insights into the neural circuitry driving stress-induced reproductive dysfunction.
86 This discovery significantly advances our understanding of how emotional stress directly impacts
87 reproductive health and identifies potential neural targets for therapeutic intervention in stress-related
88 reproductive disorders.

Results

Dynamic reconfiguration of MePD GABA neuronal networks during selective optogenetic stimulation of urocortin-3 (UCN3) neurons and restraint stress

To investigate how the posterodorsal subnucleus of the medial amygdala (MePD) processes stress signals and to understand the role of GABA and UCN3 neurons in this process, we employed *in vivo* calcium imaging using GRadient INdex (GRIN) mini-endoscopy. A cohort of six female UCN3Cre::VGAT-Flpo transgenic mice were injected with a viral mixture containing pAAV-Syn-Flexrc[Chrimson-tdTomato] and pAAV-EF1a-fDIO-GCaMP6s. This intersectional viral strategy enabled dual functionality: (i) optogenetically stimulating MePD UCN3 neurons via Chrimson; and (ii) detecting calcium activity in MePD GABA neurons using GCaMP6s (Fig. 1**A**). GRIN lenses were surgically implanted at the same location as the viral injection, enabling imaging of calcium activity with single-neuron resolution Fig. 1**B-G**). The specificity of the AAV-Syn-Flex-rc[Chrimson-tdTomato] expression in the MePD was quantified by overlapping analysis with the UCN3 immunohistochemical staining and revealed that 95.06 ± 2.24% of tdTomato-positive neurons co-localized with the UCN3 immunohistochemical positive neurons (Supplementary Fig. 1). Further, 81.61 ± 6.03% of the total UCN3-immunoreactive neurons co-expressed Chrimson-tdTomato (Supplementary Fig. 1).

Two series of experiments were conducted to assess GABAergic responses under distinct conditions. First, to assess the role of UCN3 neurons in recruiting GABAergic response, baseline calcium activity from MePD GABA neurons was recorded for 3 min, followed by 3 min of recording during optogenetic stimulation of UCN3 neurons (Fig. 1**A**). Optogenetic stimulation was delivered in a discontinuous pattern, 5 seconds on, 5 seconds off, with a light-pulse frequency of 10 Hz during the ‘on’ periods (10ms pulse width, 10 mW power, and 532 nm wavelength). GABA neurons with activity that mimics the pattern of optic stimulation, evidence that they are co-expressing UCN3, are removed from further analysis (see Methods and Supplementary Fig. 2). To further characterize the GABAergic response to acute stressors, baseline calcium activity of GABA neurons was recorded for 2 min, followed by 2 min of recording while the animals were exposed to restraint stress (Fig. 1**A**). The dynamic GABAergic response to optogenetic stimulation of UCN3 neurons and restraint stress was summarized in

116 functional terms using pairwise (neuron-neuron) association matrices, constructed from Pearson
117 correlation coefficients between neuronal trace pairs (see Methods). These correlation matrices
118 represent the MePD GABAergic response as a graph of interconnected nodes (neurons) with edge
119 weights corresponding to the strength of their pairwise functional interactions (Fig. 1**H**&**I**)[24]. To quantify
120 the effect of stress or UCN3 activation on functional connectivity we calculated the normalized
121 Riemannian distance between the correlation matrices from baseline and stimulation/stress periods.
122 Our analysis revealed significant alterations in the functional connectivity of the GABAergic network
123 during both UCN3 stimulation and stress relative to control animals lacking channelrhodopsin
124 expression (Fig. 1**J**). Furthermore, on average, stress induces a significantly higher population time-
125 averaged calcium response than UCN3 stimulation; however, this effect diminishes over the 2-minute
126 stress period (Fig. 1**K**). These results indicate that the GABA population in the MePD plays a pivotal
127 role in processing stress signals, such as those induced by restraint stress. Furthermore, our findings
128 suggest that UCN3 neurons may serve as a key relay, driving functional reorganization within the
129 GABAergic population to support transmission of stress-related information.

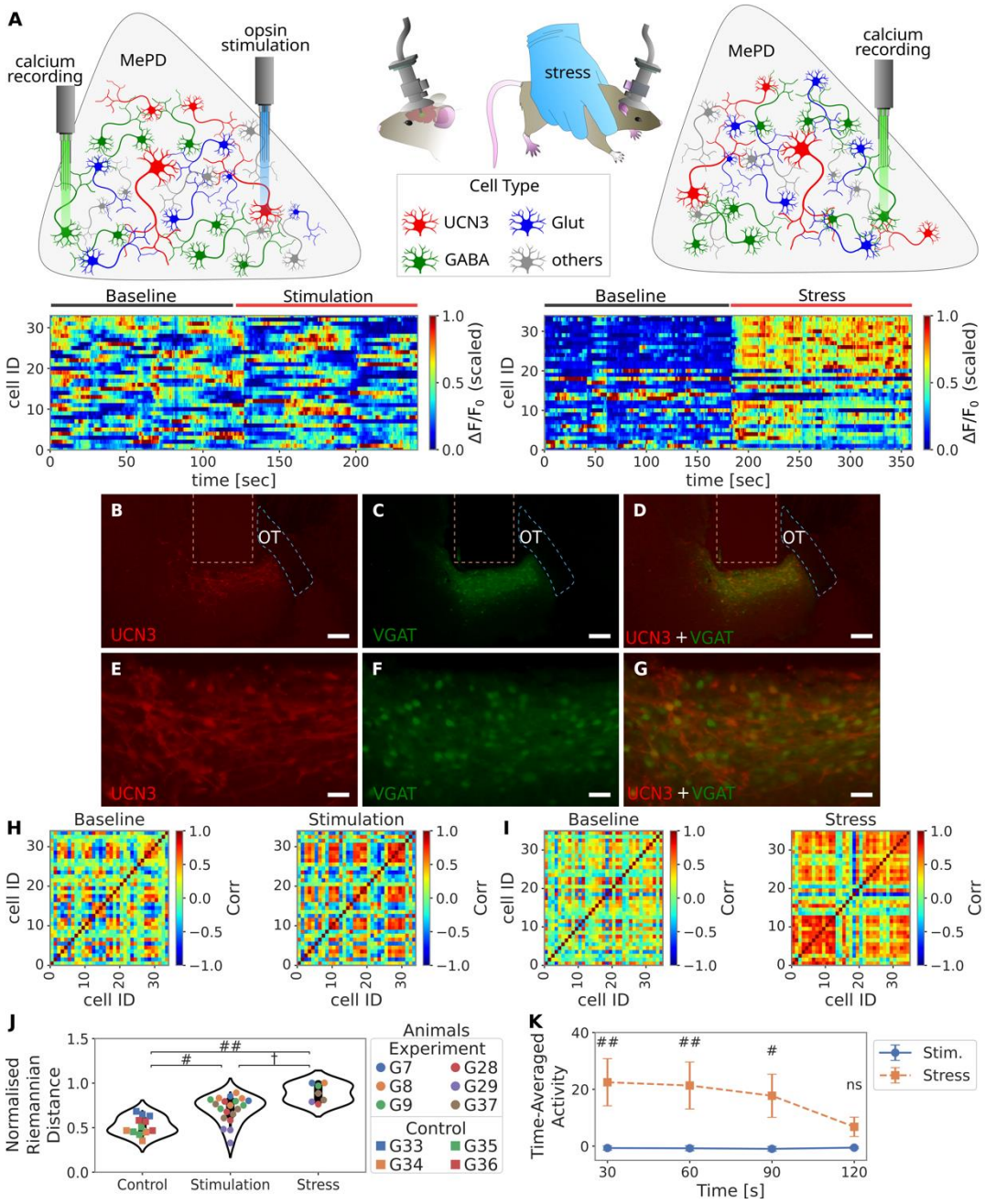

Figure 1: Functional connectivity of GABA neurons in posterodorsal medial amygdala (MePD) reconfigures in response to optogenetic stimulation of urocortin-3 (UCN3) neurons or acute restraint stress. (**A**) Schematic diagram of the experimental design for stimulating MePD UCN3 neurons and simultaneously imaging calcium activity from MePD GABA neurons. Representative heatmaps of calcium activity ($\Delta F/F_0$) recorded from MePD GABA neurons (left) in response to optogenetic stimulation of UCN3 neurons, (animal G7 trial 2, 34 neurons, see Supplementary Table 1; GABA neurons meeting our criteria for UCN3 expression excluded see Supplementary Fig. 2) and (right) during restraint-induced stress (animal G28, 35 neurons, see Supplementary Table 2). **(B-G)** Representative photomicrographs of the MePD from a UCN3-Cre::VGAT-Flpo mouse injected with pAAV-Syn-Flex-rc+pAAV-EF1a-fDIO-GCaMP6s. (**B**&**E**) Red fluorescence

140 (tdTomoato) labels UCN3 neurons expressing Chrimson-tdTomato, (**C**&**F**) green fluorescence labels GABA
141 neurons, and (**D**&**G**) red and green signals merged. (**H**&**I**) Functional connectivity matrices during baseline and
142 under UCN3 activation and stress were constructed by calculating the pairwise Pearson's correlation between
143 calcium time-traces. (**J**) Normalized Riemannian distance between the correlation matrices from baseline and
144 stimulation/stress periods. Each data point represents a single experiment, with different animals color-coded;
145 control animals are shown as squares, and channelrhodopsin-expressing animals as circles. (**K**) Difference in
146 time-averaged calcium activity between periods of UCN3 stimulation or stress and the baseline period. Scale
147 bars: **B**-**D**, 200 μm; **E**-**G**, 50 μm.

148 **Clustering analysis reveals two functionally distinct GABA subpopulations in the MePD**

149 To better understand the functional organization of the GABA MePD network during optogenetic
150 stimulation of UCN3 neurons and under restraint stress, we performed clustering analysis on the
151 functional connectivity matrices we obtained from the calcium recordings of GABA neurons.
152 Clustering results consistently revealed two functionally distinct cell populations both during
153 optogenetic stimulation of UCN3 neurons and restraint stress (Fig. 2**A**&**C**). Under both conditions,
154 activity between the two clusters appeared highly anti-correlated as illustrated by two representative
155 examples depicted in Fig. 2**B**&**D**. Moreover, we find that clusters are significantly different in size, with
156 the smallest cluster accounting on average for 35% of all cells (Fig 2**E**&**F**, Supplementary Fig. 3). The
157 robustness of the above finding was also verified using the K-means clustering algorithm and an
158 alternative measure of association between neuronal traces that accounts for time-lag and sign in
159 neuronal interactions (see Methods and Supplementary Figs. 4-6).

160 Varying the frequency of optogenetic stimulation of UCN3 neurons influenced the functional
161 connectivity within the GABA network (Supplementary Fig. 7). Stimulation at 5 Hz produced no
162 significant change compared with controls, 10 Hz resulted in a statistically significant increase, while
163 20 Hz reduced the effect, which could possibly reflect a differential release of
164 neurotransmitters/neuropeptides at higher frequencies[25]. In contrast, stimulation at 5, 10, or 20 Hz did
165 not significantly affect the correlation between the average activity of the two GABA clusters
166 (Supplementary Fig. 8). Based on the functional role of the MePD in relaying stress signals to the
167 hypothalamic arcuate nucleus (ARC), our results suggest that the identified GABA subpopulations

168 (clusters) could correspond to distinct populations of GABA interneurons and GABA efferent
169 neurons—defined as neurons that transmit signals from the MePD to downstream targets. Known
170 efferent projections to the ARC play a role in regulating the gonadotropin-releasing hormone (GnRH)
171 pulse generator, a key driver of reproductive function[11,17].

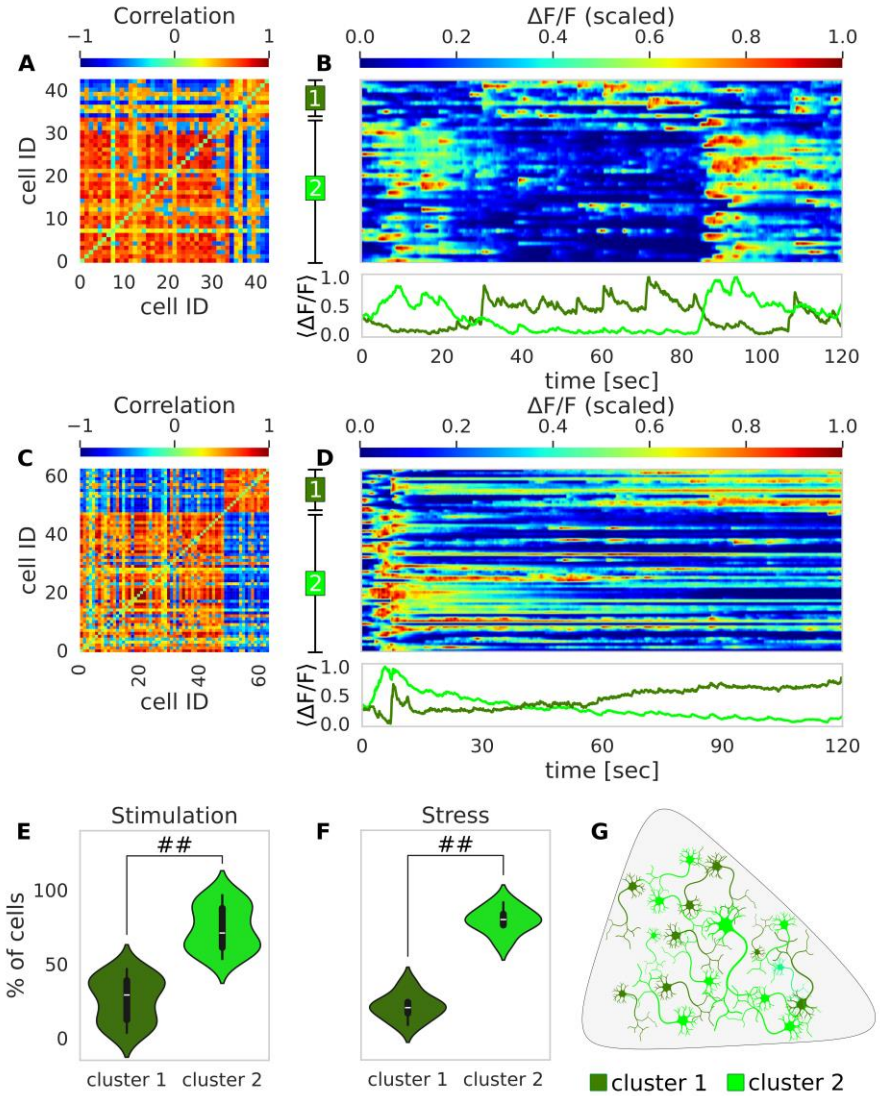

172

173 **Figure 2**: **Clustering identifies two functionally distinct GABA subpopulations in the posterodorsal**
174 **medial amygdala (MePD) both during UCN3 optogenetic stimulation and restraint stress**. Representative
175 example of (**A**) a clustered connectivity matrix and (**B**) associated calcium time-traces of MePD GABA neurons
176 during optogenetic stimulation of UNC3 neurons and the population average below. Representative examples
177 of (**C**) a clustered connectivity matrix and (**D**) associated calcium activity time-traces of MePD GABA neurons
178 during restraint stress and the average population activity below. (**E**&**G)** Relative sizes of the two GABA
179 subpopulations identified via clustering analysis. (##: $p<0.001$).

180 **Mutually inhibitory interactions between GABA populations drive anti-correlated activity**

181 To explore the network mechanisms driving the anti-correlated activity of the GABA subpopulations,
182 we build upon our previously developed MePD circuit model[11]. The model allows us to explore
183 interactions between MePD neuronal populations and understand emergent patterns of dynamical
184 activity. Specifically, the model describes the calcium dynamics of two interacting populations of GABA
185 neurons, corresponding to interneurons and efferent projection neurons. Efferent neurons project their
186 axons outside the MePD to downstream targets such as the KNDy network. Both GABA populations
187 interact with a glutamatergic population (Fig. 3**A**). Experimental evidence shows that antagonizing
188 glutamate signaling completely blocks the suppressive effect of MePD UCN3 activation on LH
189 pulsatility[23], highlighting a functional role of glutamatergic neurons in the circuit. Therefore, the activity
190 of the glutamatergic population is also included in the MePD model alongside the two GABA
191 populations. Model equations are provided in Supplementary Information, and the parameter values
192 for the MePD model are in Supplementary Table 3.

193 To incorporate input from UCN3 neurons we include a non-autonomous term in the model informed
194 by recordings of the activity of UCN3 neurons during optogenetic stimulation (see Fig. 3**A** and
195 Methods). The recorded traces exhibit a periodic pattern driven by the experimental stimulation
196 protocol with 5 seconds on, 5 seconds off (see Methods). In the model, we approximated this UCN3
197 input using a constant drive along with a sinusoidal function with roughly 5 seconds on, 5 seconds off
198 pattern, driving the populations GABA interneurons and the glutamatergic neurons. To simulate the
199 anti-correlated activity between the two GABA neuronal subpopulations while also reproducing
200 previously published results on the effects of neuropharmacological perturbations in the MePD on LH
201 pulsatility[23], we find that we need to include bi-directional (i.e. mutually inhibitory) GABA interaction in
202 the circuit as well as GABA interneurons self-inhibition (Fig. 3**A**).

203 Next, we validate our model by simulating the effects of stress on the MePD circuit. UCN3 neurons in
204 the MePD have also been shown to mediate psychosocial stress-induced suppression of the GnRH
205 pulse generator[16]. Experimentally recorded calcium activity of UCN3 neurons during stress
206 intervention is characterized by a fast rise followed by a slow decay (Fig. 3**B**), which we model by

taking the difference between two exponential functions, with one fast and one slow time constant (see Methods). Using this input, our mathematical model confirms the emergence of anti-correlated behavior between the GABA subpopulation whereby the activity of GABA interneurons decreases over the stress period, while the activity of the GABA efferent neuron population increases (Fig. 3**B**), supporting the proposed MePD circuit structure (Fig. 3**A**).

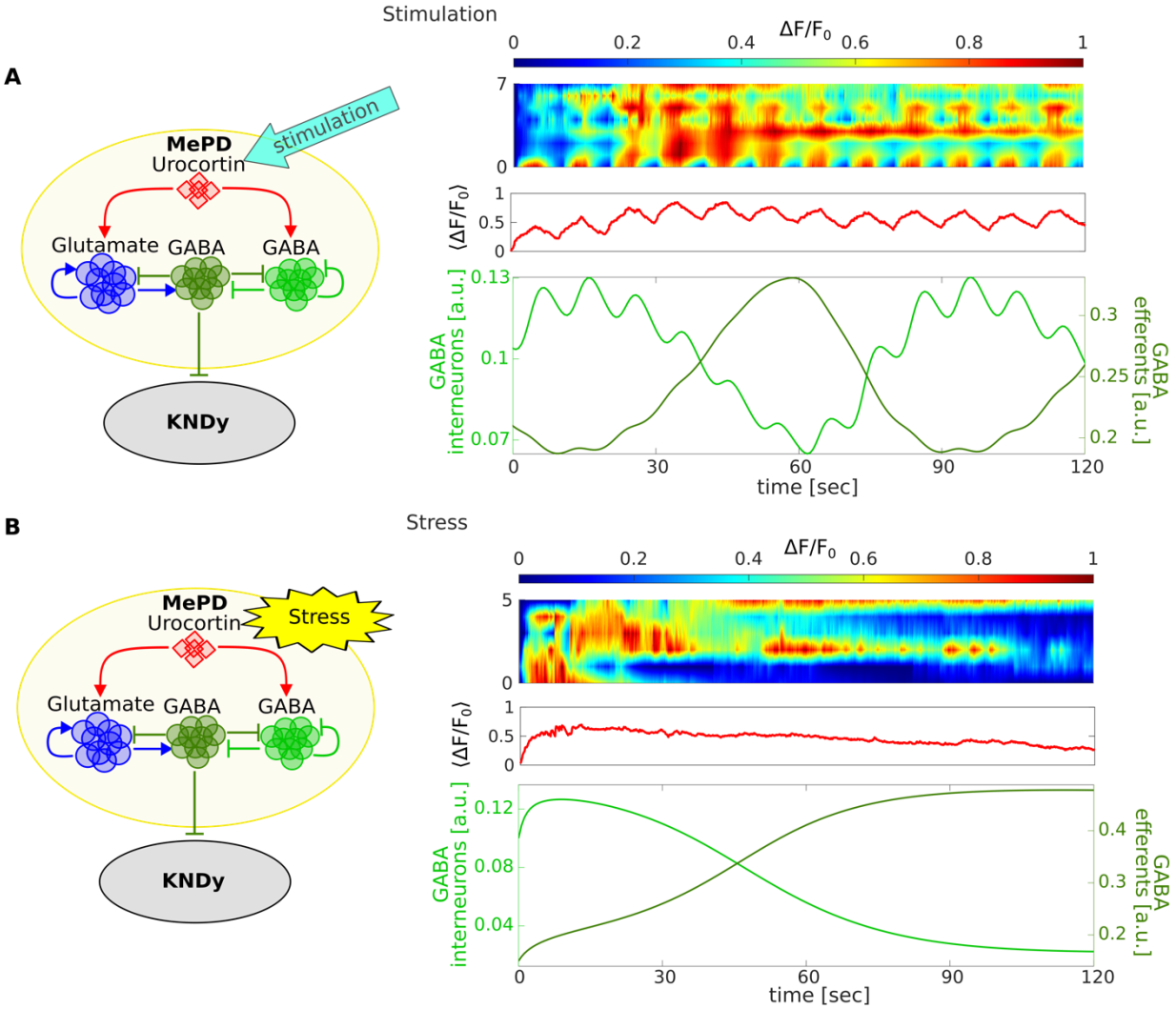

Figure 3: Mathematical model simulating the activity in the GABA neuronal populations in the MePD under the increased excitatory input from UCN3 neurons and mimicking the conditions under restraint stress. The schematics on the left provide a visual representation of the assumptions built into our mathematical model of the MePD neuronal circuit, consisting of two GABA populations and a glutamatergic population, that interact with UCN3. **(A)** Calcium time-traces of MePD UCN3 neurons during optogenetic stimulation of UCN3 neurons and corresponding mean activity. Model simulations of the effects of UCN3 optogenetic stimulation supports the emergence of anti-correlated activity in GABA subpopulations. **(B)** Calcium time-traces of MePD

220 UCN3 neurons during restraint stress and corresponding mean activity of the UCN3 calcium traces during
221 restraint stress with corresponding mean activity. Simulations of the MePD circuit under the effects of stress also
222 support anti-correlated GABA subpopulations' activity.

223 ***In silico* modeling reveals complementary relationship between MePD GABA and UCN3**
224 **populations**

225 Having shown that the model of the MePD circuitry reproduces the observed anti-correlated dynamics,
226 we next couple it to our network model of the KNDy population[11,26]. KNDy model details are in
227 Supplementary Information, and the model parameter values can be found in Supplementary Table
228 4. Since KNDy neuronal activity serves as a well-established proxy for LH secretion, we use the
229 dynamics of the KNDy network model to infer changes in LH pulsatility in response to MePD circuit
230 manipulations. Our previous in silico findings[11] show that MePD signal integration is predominately
231 mediated by GABA projections. The effects of MePD GABA and glutamate antagonism alone and
232 together with UCN3 stimulation on LH pulsatility have been previously investigated[23], and we use
233 these experimental findings to calibrate our coupled model parameters by reproducing these effects
234 accordingly (see Supplementary Fig. 9).

235 Next, using the calibrated model, we predict that providing a periodic excitatory input (see
236 Supplementary Fig. 10**A**), that mimics the effects of optogenetic stimulation of UCN3, leads to the
237 increase in the KNDy inter-pulse interval (IPI) from 15.18 min to 23.97 min due to increased activity
238 in the inhibitory GABAergic input to the KNDy network (Fig. 4**A**).

239 Since MePD has an overwhelming number of GABAergic outputs and interneurons, we are interested
240 in their role in information processing of stress signaling. To this end we provide periodic excitatory
241 input directly to both populations of GABA neurons (see Methods and Supplementary Information).
242 This is different to the indirect activation through UCN3 stimulation, as it leads to the increased activity
243 in both GABA subpopulations (Supplementary Fig. 10**B**). The resulting effect on the KNDy IPI is an
244 increase from 15.18 min to 42.65 min (Fig. 4**B**).

245 In the model we hypothesize that UCN3 signaling to the KNDy is operating through the GABAergic
246 pathway, hence disrupting GABAergic interactions will suppress UCN3's effects on KNDy. To

247 investigate it we suppress the strength of the GABAergic interactions by 50% and mimic UCN3
248 stimulation by providing excitatory input to the circuit. The model shows that this intervention does not
249 have a significant effect on KNDy IPI, apart from slightly increasing it from 15.18 min to 17.31 min
250 (Fig. 4**C** & Supplementary Fig. 10**C**).
251 Taken together the above could be summarized as the following set of model predictions along with
252 suggested ways to test them experimentally:

253 1. Optogenetic stimulation modelled via excitation of the MePD UCN3 increases the KNDy IPI
254 15.18 min to 23.97 min. This could be tested experimentally via in vivo optogenetic activation
255 of the MePD UCN3 neuronal population and simultaneous measurement of LH pulsatility.
256 2. Stimulation of the MePD GABA populations increases the KNDy IPI 15.18 min to 42.65 min.
257 Such a substantial change underscores the critical role of GABAergic signaling in modulating
258 KNDy pulsatility. Experimental confirmation could involve in vivo optogenetic activation of the
259 entire MePD GABA population accompanied by LH pulsatility measurement.

260 3. Stimulation of the MePD UCN3 with simultaneous suppression of the GABAergic interactions
261 in the MePD does not significantly affect KNDy IPI, changing it from 15.18 min to 17.31 min.
262 This finding suggests that UCN3 effects on the KNDy network are primarily dependent on its
263 interactions with GABA populations. A strategy to verify this hypothesis experimentally could
264 be to stimulate UCN3 non-GABA-expressing neurons in vivo while simultaneously inhibiting
265 non-UCN3 GABA neurons and measure LH pulsatility.

266 Finally, we investigate in silico the effects of stress on LH pulse dynamics mediated via the MePD. In
267 the restraint-stress experiment it was shown that one GABA cluster was active, while the other one
268 was inactive (Fig. 2**D**). By simulating these dynamics (Supplementary Fig. 9**D**) in the coupled MePD
269 - KNDy network model we are able to demonstrate that pulses in the KNDy network ceased (Fig. 4**D**).
270 These modeling findings align with published experimental evidence indicating that restraint stress
271 suppresses LH pulsatility[16].

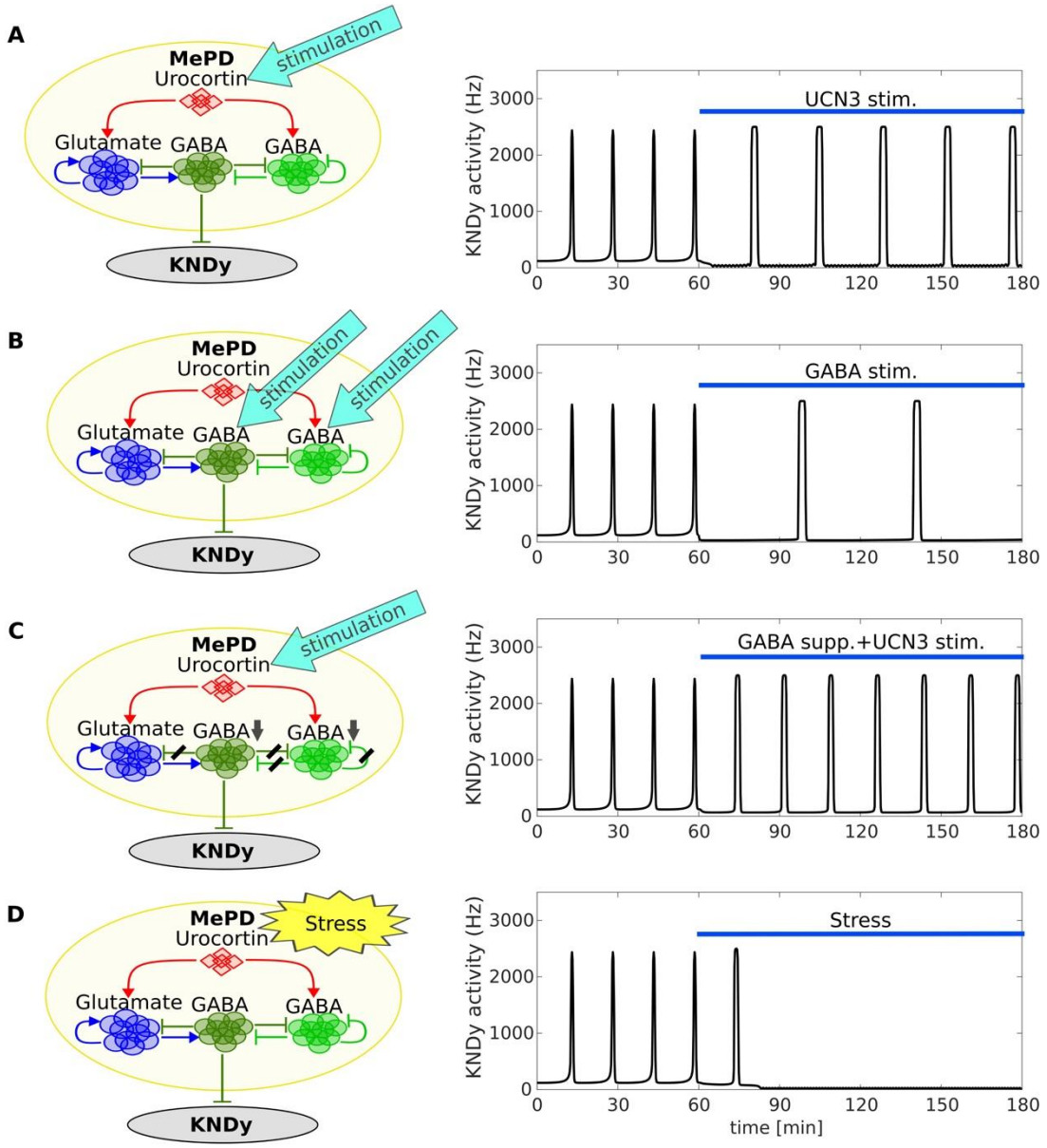

Figure 4: Coupled MePD - KNDy model predictions for the effect of stress and stimulation of UCN3 neurons on GnRH pulse generator activity and hence LH pulsatility. (**A**) Simulation of the optogenetic stimulation of the UCN3 neurons leads to the increase of the KNDy IPI 15.18 min to 23.97 min. (**B**) Mimicking the effects of the optogenetic stimulation of the MePD GABA neurons *in silico* (providing excitatory input to both GABA populations) increases KNDy IPI from 15.18 min to 42.65 min. (**C**) Simulation of the effects of the optogenetic stimulation of the UCN3 neurons and simultaneous inhibition of GABA neuronal populations do not significantly affect KNDy IPI, where it changes from 15.18 min to 17.32 min. (**D**) Simulating the effects of stress leads to the cessation of the pulsatile dynamics.

281 **Selective optogenetic stimulation of UCN3 non-GABA neurons inhibits pulsatile LH secretion**
282 **in female mice.**

283 We now test experimentally our modeling predictions detailed in the previous section regarding the
284 inhibitory effect of MePD UCN3 activation on LH pulsatility in vivo in freely behaving mice. To this end
285 a cohort of UCN3-Cre::VGAT-Flpo transgenic female mice was injected with an AAV-nEF-Con/Foff
286 2.0-ChRmine-oScarlet viral construct. This intersectional approach enabled conditional expression of
287 channelrhodopsin (ChRmine) in UCN3 neurons not expressing GABA (UCN3 non-GABA) (Con/Foff
288 group). Following the viral injection, a unilateral fiber-optic cannula was implanted into the MePD,
289 above the injection site, to facilitate selective activation of the targeted neuronal population. The
290 specificity of the AAV-nEF-Con/Foff 2.0-ChRmine-oScarlet expression in the MePD was quantified by
291 overlapping analysis with the UCN3 immunohistochemical staining and revealed that 98.92 ± 1.08%
292 of the oScarlet-positive neurons co-localized with the UCN3 immunohistochemical positive neurons
293 (Supplementary Fig. 11). Further, 54.18 ± 5.04% of the total UCN3-positive neurons coexpressed
294 ChRmine-oScarlet (Supplementary Fig. 11).

295 The stimulation protocol consisted of a 60-min control period, followed by 60 min of optogenetic
296 stimulation. Stimulation was delivered, as above, in a pulsed pattern (5 seconds on, 5 seconds off)
297 with a pulse frequency of 10 Hz during the on period (10-ms pulse width, 10 mW power, 532 nm
298 wavelength). Blood samples (5 μL) were collected every 5 min throughout the protocol and used to
299 measure LH levels.

300 Statistical analysis indicated post-stimulation LH inter-pulse intervals differed across the two groups
301 ($F(2, 30) = 15.83$, $P < 0.0001$; two-way ANOVA). In the Con/Foff group, the LH inter-pulse interval
302 significantly increased after optogenetic stimulation compared to the control period (15.47 ± 0.91 min
303 vs. 23.75 ± 1.07 min, mean ± SEM, n = 6, $p<0.01$; Fig. 5**A**&**D)**, validating the first of our modeling
304 predictions. In contrast, the no-stimulation group, which received the Con/Foff viral construct without
305 optogenetic stimulation, showed no significant changes in LH inter-pulse interval (15.84 ± 0.37 min
306 vs. 16.68 ± 0.86 min, n = 6, $p > 0.05$; Fig. 5**B**&**D**). Similarly, in a separate cohort of mice injected with
307 a control virus (DIO-EYFP), optogenetic stimulation resulted in no significant differences in LH inter-

308 pulse intervals before and after stimulation (19.83 ± 1.02 min vs. 17.78 ± 0.93 min, n = 6, p > 0.05;
309 Fig. 5**C**&**D**). The LH pulse amplitude and mean LH levels were quantified, and data are provided in
310 Supplementary Table 5.

311 **Selective optogenetic stimulation of UCN3-expressing GABA neurons fails to affect pulsatile**
312 **LH secretion in female mice.**

313 To further test the functional interactions between the UCN3 and GABA populations, a separate cohort
314 of UCN3-Cre::VGAT-Flpo transgenic female mice was injected with an AAV-nEF-Con/Fon
315 2.0ChRmine-oScarlet viral construct, which allows optogenetic stimulation of UCN3 neurons
316 coexpressing GABA (UCN3-expressing GABA) (Con/Fon group). The specificity of the AAV-
317 nEFCon/Fon 2.0-ChRmine-oScarlet expression in the MePD was quantified by overlapping analysis
318 with the UCN3 immunohistochemical staining and revealed that 98.77 ± 1.24% of the oScarlet-positive
319 neurons co-localized with the UCN3 immunohistochemical positive neurons co-expressing GABA
320 (Supplementary Fig. 12). Further, 32.73± 2.60% of the total UCN3-positive neurons co-expressed
321 ChRmine-oScarlet (Supplementary Fig. 12).

322 Statistical analysis showed no significant interaction effect of group and optogenetic stimulation on LH
323 inter-pulse intervals (F (1, 18) = 0.2709, p = 0.6091; two-way ANOVA). That is, LH inter-pulse intervals
324 in the Con/Fon group, showed no change following optogenetic stimulation compared to the control
325 period (17.92 ± 0.80 min vs. 16.60 ± 0.88 min, mean ± SEM, n = 6, p > 0.05; Fig. 5**H**&**J**). Similarly, in
326 the no-stimulation control experiment for this cohort, which did not receive optogenetic stimulation,
327 there was no significant difference in LH inter-pulse intervals (16.08 ± 1.45 min vs. 15.83 ± 0.95 min,
328 n = 5, p > 0.05; Fig. 5**I**&**J**). The LH pulse amplitude and mean LH levels were quantified, and data are
329 provided in Supplementary Table 5.

330 Taken together, our results suggest that although UCN3 and GABAergic neuronal populations overlap,
331 they serve distinct functional roles within the MePD circuit, with both being critical for relaying inhibitory
332 signals to the hypothalamic GnRH pulse generator. While independent activation of either population
333 inhibits the GnRH pulse generator, activation of UCN3 neurons that co-express GABA is insufficient
334 to elicit this effect.

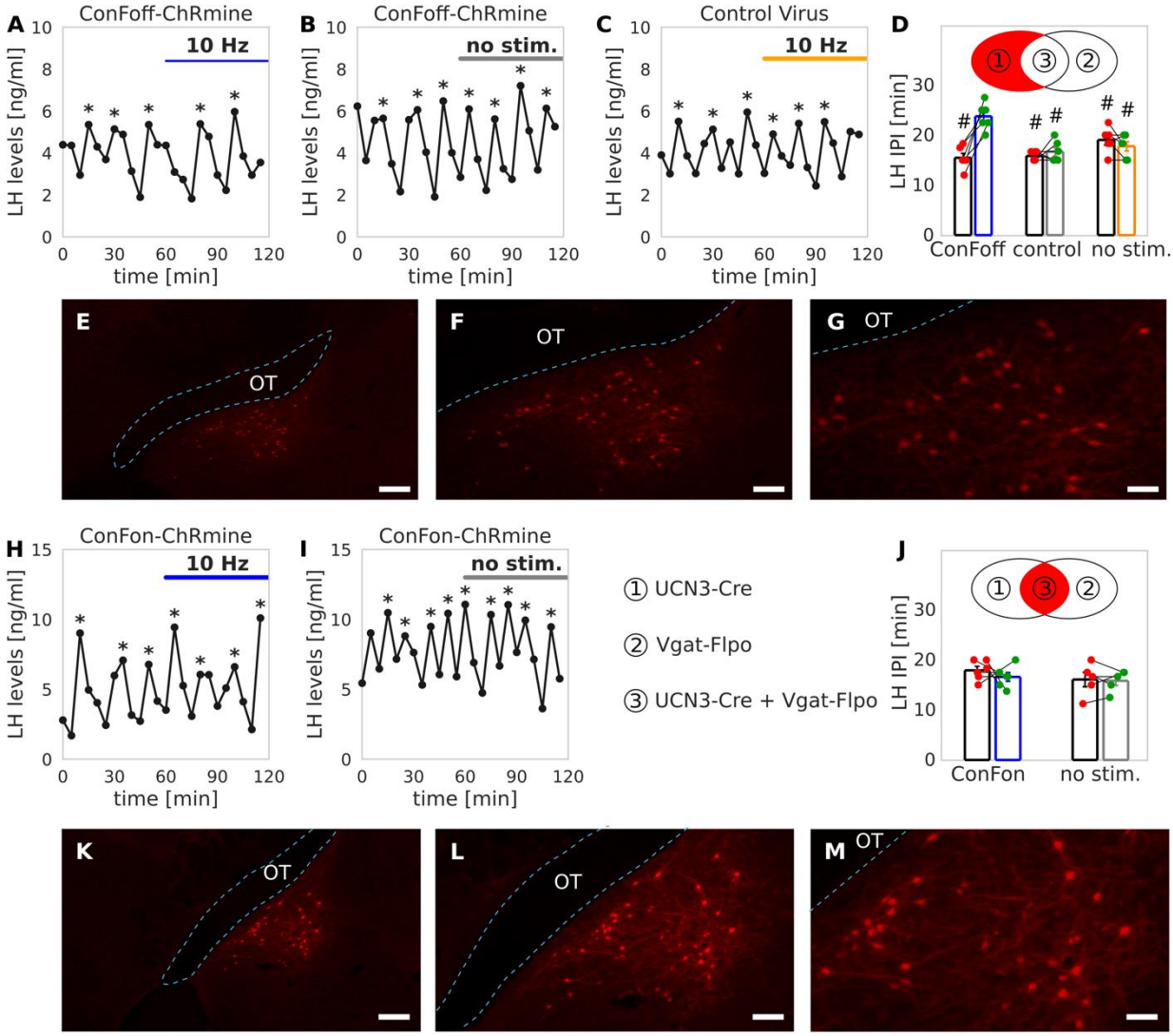

Figure 5: Effect of optogenetic stimulation of UCN3 non-GABA and UCN3 neurons co-expressing GABA in the MePD on LH pulse frequency. (**A**-**D**) Optogenetic stimulation of UCN3 non-GABA neurons inhibited LH pulses. Representative examples of LH pulsatility in UCN3-Cre::VGAT-Flpo mice injected with AAV-Con/FoffChRmine in response to (**A**) 10Hz optic stimulation or (**B**) no stimulation as control, and (**C**) in mice injected with control virus in response to 10 Hz stimulation. Pulses detected by the DynPeak algorithm are indicated with an asterisk (*). (**D**) Mean LH inter-pulse interval (IPI) (±SEM) for each group during the control period and over the subsequent stimulation period. #: $p<0.01$ vs stimulation period in Con/Foff group (two-way ANOVA, Tukey's post-hoc). (**E**-**G**) Representative photomicrographs of expression of AAV-nEF-Con/Foff 2.0-ChRmine-oScarlet (red) in MePD UCN3 neurons. (**H**-**M**) Optogenetic stimulation of neurons co-expressing UCN3 and GABA in the MePD did not impact LH pulse significantly. Representative examples of LH pulsatility in UCN3-Cre::VGATFlpo mice injected with Con/Fon-ChRmine-oScarlet virus in response to (**H**) 10 Hz optic

347 stimulation or (**I**) no stimulation as control. (J) Mean LH IPI (±SEM) for each group during the control period and
348 over the subsequent stimulation period (two-way ANOVA). (**K**-**M**) Representative photomicrographs of neurons
349 co-expression UCN3 and GABA, tagged with oScarlet (red). Scale bars represent (**E**&**K**) 200 µm, (**F**&**L**) 100 µm,
350 (**G**&**M**) 50 µm. OT, optic track. The blue vertical bars in E to G and K to M indicate the position of the fiber optic
351 cannula.

352 **The MePD GABA neurons relay information from UCN3 neurons and inhibit the GnRH pulse**
353 **generator.**

354 To test our remaining model predictions and establish the functional role of GABA neurons in the
355 MePD in transmitting inhibitory signals to the hypothalamic GnRH pulse generator, we injected the
356 AAV-EF1a-DIO-ChR2-EYFP viral construct into VGAT-Cre transgenic mice, targeting the entire MePD
357 GABA neuron population for expressing ChR2 and used the optogenetic stimulation protocol
358 described above (60 min control period followed by 60 min stimulation) to stimulate the entire MePD
359 GABA population. In the VGAT-Cre-tdtomato mice, we observed that 93.27 ± 2.99% of the EYFP
360 positive neurons were tdtomato-positive and 87.01± 5.21% of the tdtomato-positive neurons were
361 EYFP-positive. This indicates a high degree of co-expression consistency between the viral and
362 transgenic reporters. Statistical analysis showed a significant interaction effect of our genetic
363 intervention and stimulation period on LH pulsatility ($F(2, 24) = 10.55$, $p = 0.0005$; two-way ANOVA).
364 Stimulation of the GABA population markedly increased the LH inter-pulse interval compared to the
365 pre-stimulation control period (18.5 ± 2.03 min vs 49.5 ± 8.46 min, mean ± SEM, $n = 5$, $p<0.01$; Tukey's
366 post-hoc; Fig. 6**A**&**D**), validating modeling prediction 2. In contrast, mice that did not receive
367 optogenetic stimulation showed no change in LH inter-pulse interval (21.25 ± 3.79 min vs 19.33 ± 1.52
368 min, $n = 5$, $p > 0.05$; Tukey's post-hoc; Fig. 6**B**&**D**). Similarly, control virus (AAV-EF1a-DIO-EYFP)
369 injections did not result in any significant difference in LH inter-pulse interval before and during
370 stimulation (16.50 ± 0.67 min vs 18.00 ± 0.62 min, $n = 5$, $p > 0.05$; Tukey's post-hoc; Fig. 6**C**&**D**). The
371 LH pulse amplitude and mean LH levels were quantified, and data are provided in Supplementary
372 Table 6.

373 Next, UCN3-Cre::VGAT-Flpo transgenic females were injected with an intersectional viral mixture
374 containing AAV-nEF-Con/Foff 2.0-ChRmine-oScarlet and pAAV-nEF-Coff/Fon-NpHR3.3-EYFP ,
375 enabling simultaneous excitation of UCN3 non-GABA neurons and inhibition of non-UCN3 GABA
376 neurons. Statistical analysis showed no significant interaction effect of genetic manipulation and
377 stimulation period on LH pulsatility ($F(1,18) = 0.131$, $p = 0.7216$; way ANOVA). Moreover, optogenetic
378 stimulation resulted in no significant change in the LH inter-pulse interval relative to the control period
379 (16.67 ± 1.31 min vs 18.61 ± 1.58 min, mean ± SEM, $n = 6$, $p > 0.05$; Fig. 6**H**&**J**), which aligns with
380 our modeling prediction 3. Similarly, in mice injected with the same viral mixture but without receiving
381 optogenetic stimulation, no significant change in LH inter-pulse interval was detected (16.33 ± 1.19
382 min vs 17.33 ± 0.81 min, $n = 5$, $p > 0.05$; Fig. 6**I**&**J**). The LH pulse amplitude and mean LH levels were
383 quantified, and data are provided in Supplementary Table 5.

384 Collectively, these findings suggest that MePD GABA neurons are integral to regulating LH pulse
385 frequency. The inhibitory effect on LH pulses observed upon UCN3 neuron activation is attenuated
386 when GABA neuron activity is optogenetically suppressed, implying that GABA signaling acts
387 downstream of UCN3 neurons, relaying the inhibitory signal to the hypothalamic GnRH pulse
388 generator.

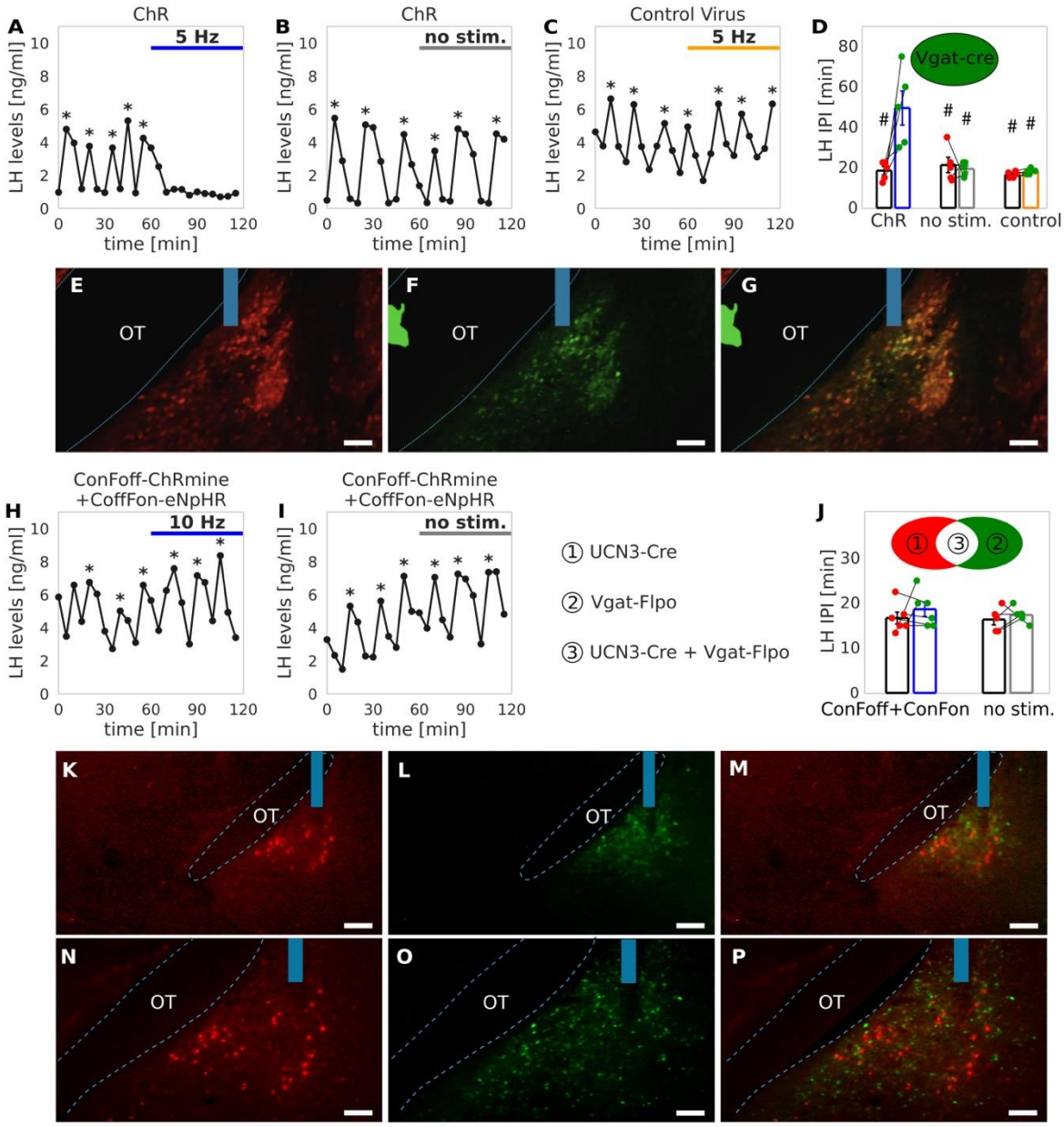

389

390 **Figure 6: Selective optogenetic stimulation of GABA neurons in the MePD inhibits LH pulsatility and**
391 **their activity is necessary for mediating UCN3 signaling downstream.** (**A-G**) Optogenetic activation of the
392 entire MePD GABA population in VGAT-Cre mice led to significant LH pulse suppression. Representative
393 examples showing LH pulsatility in VGAT-Cre mice injected with AAV-double floxed-ChR2-EYFP virus in
394 response to (**A**) 5 Hz stimulation or (**B**) no stimulation as control, and (**C**) 5 Hz stimulation in mice injected with
395 control virus. (**D**) Mean LH IPI (±SEM) for each group during the control period and over the subsequent
396 stimulation period. #: p<0.01 vs stimulation period in ChR2 group (two-way ANOVA, Tukey's post-hoc). (**E-G**)
397 Representative photomicrographs of MePD GABA neurons, labeled with (**E**) tdTomato (red), (**F**) ChR2-EYFP

398 (green), and (**G**) merged. Scale bars represent. (**H-P**) The simultaneous inhibition of non-UCN3 GABA neurons
399 in the MePD restored the LH suppression induced by stimulation of non-GABA UCN3 neurons. Representative
400 examples showing LH pulsatility in UCN3-Cre::VGAT-Flpo female mice injected with Con/FoffChRmine-oScarlet
401 and Coff/Fon-NpHR-EYFP virus mixture in response to (**H**) 10 Hz optogenetic stimulation or (**I**) no stimulation as
402 control. (**J**) Mean LH IPI (±SEM) for each group during the control period and over the subsequent stimulation
403 period. (two-way ANOVA). (**K-P**) Representative photomicrographs of fluorescence in MePD neurons. (**K**&**N**)
404 non-GABA UCN3 neurons tagged with oScarlet (red), (**L**&**O**) non-UCN GABA neurons tagged with EYFP (green)
405 (**M**&**P**) merged. Scale bars represent (**E-G**) 150 µm, (**K-M**) 200 µm, (**N-P**) 100 µm. OT, optic track. The blue
406 vertical bars in **E** to **G** and **K** to **P** indicate the position of the fiber optic cannula.

407 ## Discussion

408 The posterodorsal subnucleus of the Medial Amygdala (MePD) is a critical regulator of reproductive
409 function. Single-cell transcriptomics has revealed a mosaic of glutamatergic and GABAergic
410 populations in this region, with GABA neurons co-expressing receptors for gonadal steroids as well
411 as neuromodulators and cognate receptors involved in parental and sociosexual behavior (including
412 kisspeptin, prolactin and oxytocin)[27]. Furthermore, calcium imaging of neuronal ensembles from this
413 region has started to decipher how this brain region encodes information about social interactions and
414 stressful stimuli[28], with stress-related information being relayed to the reproductive axis via potentially
415 direct projections to the hypothalamus[1,2], and eliciting well-documented responses in pubertal
416 timing[12,13], LH secretion[16,17] and the GnRH pulse generator[9–11]. Here, to elucidate the neuronal circuitry
417 involved in MePD processing of stress signals, we used GRIN lens mini-endoscopic calcium imaging
418 to study, for the first time, the dynamic activity of MePD GABA neurons under acute restraint stress
419 as well as the activity of GABA neurons in response to UCN3 activation. Functional network analysis
420 of the imaging data revealed that acute restraint stress induces a reconfiguration of the GABA
421 population, highlighting their role in encoding and transmitting stress information. Optogenetic
422 stimulation of UCN3 neurons produced a comparable network reconfiguration indicating that both
423 populations are co-involved in stress processing. The overall magnitude of calcium activity ($\Delta F/F_0$)
424 differed between the two conditions, with stress generally inducing a stronger response than

425 optogenetic stimulation of UCN3 neurons. This discrepancy may reflect the engagement of additional
426 stress-related pathways or neuromodulatory factors that are not fully replicated by isolated UCN3
427 stimulation, such as stress-induced GABA transmission that has been well-documented in the
428 amygdala[17,23]. Clustering analysis of the calcium transients identified two distinct GABA
429 subpopulations with anti-correlated activity. This finding of two distinct populations is consistent with
430 physiological and morphological studies of GABA neurons in the medial amygdala characterizing them
431 as either projecting cells or local[18,20].

432 Building upon our previously developed computational model of the MePD circuit, we explored the
433 network connectivity to understand the possible mechanisms through which anti-correlated activity
434 emerges. The model consists of a glutamatergic subpopulation and two GABA subpopulations: one
435 comprising GABA interneurons and the other GABA efferent projection neurons. Our analysis
436 identified two conditions necessary for the emergence of anti-correlated activity between these GABA
437 subpopulations, consistent with our experimental observations. First, mutual inhibition between the
438 GABA subpopulations is required, such that activation of one population suppresses the other. In our
439 mechanistic model, mutual inhibition arises from the biophysical characteristics of GABAergic
440 transmission, where the release of GABA inhibits target neurons, thereby producing inhibitory
441 interactions between the subpopulations. Second, if both subpopulations receive a shared input (e.g.,
442 from the glutamatergic population or any other population of excitatory cells), their dynamics become
443 entrained to that common stimulus, meaning that distinct input streams to each subpopulation are
444 necessary for the observed anti-correlation. To satisfy this condition in our model, GABA interneurons
445 receive inputs from UCN3 neurons, whereas the GABA efferent projection neurons receive inputs
446 from the glutamatergic population. This circuitry implies that stress information is processed along two
447 key pathways (one glutamatergic and one GABAergic) and is integrated by the GABA efferent
448 projection neurons to the arcuate KNDy system.

449 We note that an alternative connectivity pattern, with the UCN3 population directly projecting to the
450 GABA efferent population, could also fit our experimental observations, but would not reproduce
451 previously published results on the effects of neuropharmacological perturbations in the MePD on LH

452 pulsatility[23]. Specifically, the suppression of glutamatergic neurons in combination with stimulation of
453 UCN3 neurons. Under this scenario, direct input from stimulated UCN3 to GABA efferent neurons will
454 lead to the increase in its activity, consequently increasing KNDy inter-pulse interval (IPI). This finding
455 contrasts with experimental observations, where the combined suppression of glutamate and
456 stimulation of UCN3 failed to produce any significant change in GnRH pulsatility[23].

457 Additionally, UCN3 neurons may co-release other fast neurotransmitters, such as glutamate[27]. The
458 result of our UCN3 neurons stimulations at low frequencies (5 Hz; Supplementary Fig. 7), which
459 primarily elicits the fast neurotransmitters release[25], suggests that their isolated effects may be limited.
460 We note that in our modeling framework, we include the constant drive, reflecting the effects of slow
461 neuropeptide action, and a periodic drive corresponding to the action of fast neurotransmitters aligned
462 with the stimulation frequency. The constant drive governs the overall dynamical regime, while the
463 fast periodic term functions primarily as a rhythmic modulator, that is when the periodic drive
464 dominates over the constant drive both the glutamatergic and GABAergic populations become
465 entrained to the stimulation frequency. Nonetheless the specific contribution of co-transmitters
466 remains experimentally unclear, and that may influence how the MePD integrates this tonic input (Fig.
467 7).

468 We note that our MePD model has potential applications beyond understanding MePD dynamics and
469 their influence on the GnRH pulse generator. The model incorporates two functionally distinct
470 populations of GABA neurons (interneurons and efferent projection neurons), which reflect known
471 differences in GABA neurons within the amygdala[18,20]. This diversity likely originates from the medial
472 ganglionic eminence an embryonic structure that gives rise to GABA interneuron populations across
473 various brain regions, including the MePD, through migration during embryogenesis[29]. Therefore, our
474 modelling framework could be extended to other neural circuits where two functionally distinct GABA
475 populations exist, such as the posterior ventral medial amygdala[20] and its lateral and basal
476 subdivisions[30].

477 Consistent with model predictions, we showed that optogenetic activation of non-GABA neurons,
478 expressing UCN3, suppresses LH pulse frequency. This finding corroborates previous work

479 demonstrating that LH pulses are inhibited by activation of UCN3 neurons[13,23] or administration of
480 UCN3[16] in the MePD, and that such effects are attenuated by chemogenetic inhibition of UCN3
481 neurons or by antagonizing corticotropin-releasing factor type 2 receptors (CRFR2)[16]. Thus, our
482 findings further support the central role of UCN3 signaling in modulating both stress responses and
483 reproductive function. Future studies could investigate the contribution of UCN3 neurons to stress
484 integration more directly, for example by silencing UCN3 neurons during stress exposure to determine
485 whether GABAergic activation and the associated network clustering patterns are abolished.

486 GABA is one of the primary inhibitory neurotransmitters in the nervous system. Previous work has
487 shown that MePD GABA neurons project to the ARC to regulate LH pulses and chemogenetic
488 inhibition of MePD GABA neurons attenuates stress-induced suppression of LH pulses[17]. Here, we
489 found that optogenetic activation of GABA neurons in the MePD leads to robust LH pulse suppression,
490 reinforcing the pivotal role of amygdala GABAergic signaling in stress-related reproductive
491 dysfunction. Antagonizing GABA receptors in the MePD can block UCN3-induced LH suppression[23],
492 suggesting that GABA neurons may function downstream of UCN3 signaling.

493 However, this pharmacological approach lacks cell-type specificity, leaving open the possibility that
494 UCN3 neurons themselves co-expressing GABA receptors, potentially contributing to the observed
495 effect. Here, by using an intersectional genetic strategy, we demonstrated that optogenetically
496 inhibiting non-UCN3 GABA neurons can abolish the change in LH pulse intervals induced by
497 optogenetic stimulation of UCN3 neurons. This finding supports the hypothesis that these GABA
498 neurons are acting downstream of UCN3 signaling, mediating LH pulse suppression. We note that
499 while in our current experimental protocol we could also be blocking GABAergic projections to the
500 ARC KNDy population, which by itself could explain the absence of any effect from UCN3 stimulation,
501 our modeling predicts that GABAergic interactions within the MePD are additionally crucial for relaying
502 UCN3 signals to the KNDy network as also suggested by pharmacologically antagonizing
503 GABAreceptors[23].

504 It is not unusual for neurons to co-express and co-release neuropeptides and neurotransmitters[20].
505 Here, our statistical analysis (Supplementary Fig. 2 & Supplementary Table 1) of GABA calcium traces
506 indicate that certain GABA neurons exhibit activity entrained to the stimulation frequency of UCN3
507 neurons, suggesting a possibility that UCN3 is co-released with GABA. Given that activating either
508 UCN3 or GABA neurons independently suppresses LH pulses, one might predict that stimulating
509 neurons co-expressing both UCN3 and GABA would similarly inhibit LH. However, we observed no
510 significant changes in LH pulses upon optogenetic stimulation of neurons co-expressing UCN3 and
511 GABA. Our results indicate that UCN3 and GABA are both essential for transmitting inhibitory signals
512 to the hypothalamic GnRH pulse generator; however, this inhibitory influence relies on their action
513 through separate, functionally distinct neuronal populations. That is activation of neurons that
514 exclusively express either UCN3 or GABA suppresses the GnRH pulse generator, whereas activation
515 of UCN3 neurons that also co-express GABA fails to produce this inhibitory effect. Within our modeling
516 framework, UCN3/GABA co-expressing neurons might be considered part of the GABA interneuron
517 population, primarily inhibiting GABA projection neurons rather than activating them. Consequently,
518 they fail to relay the inhibitory UCN3 signal to the ARC. Further studies are necessary to define more
519 precisely the distinct role of UCN3/GABA co-expressing neurons within the MePD circuitry.

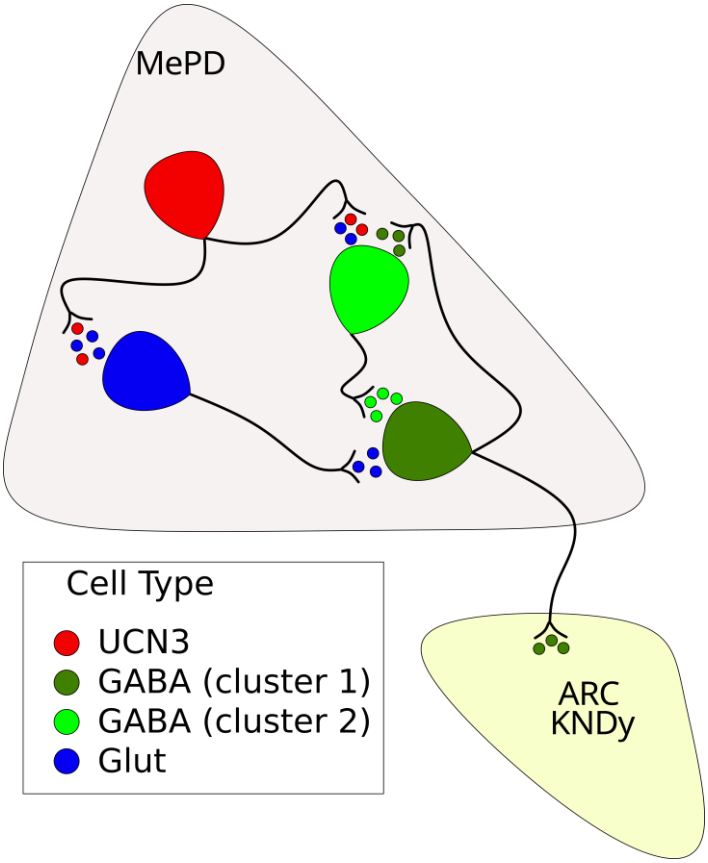

Figure 7: Schematic illustration of the proposed functional MePD neurocircuit. UCN3 neurons activate inhibitory GABA interneurons and excitatory glutamate neurons through the release of UCN3 and potentially other fast neurotransmitters. The glutamate and GABA interneuron populations then signal to the GABA efferent projection neurons, that convey the MePD output to the KNDy neurons in the arcuate nucleus.

By combining mini-endoscopic calcium imaging with computational modeling, we identified two GABA subpopulations with complementary but distinct roles in encoding stress signals and modulating LH pulsatility. Our experimental and computational results also stressed the functional orthogonality between UCN3 and GABA signaling in MePD, highlighting the complexity of the MePD's contribution to stress-induced reproductive suppression. These results offer improved understanding of the neuronal circuits in the amygdala, a key hub for emotional processing, involved in regulating hypothalamic GnRH pulse generator frequency[9–11,16,17,23] providing new insight into psychogenic stress-related disorders of fertility, such as functional hypothalamic amenorrhoea[6,7,31,32], and the development of novel therapeutic approaches to improve reproductive health and well-being.

534 # Methods

535 **Animal**

536 VGAT-Cre-tdTomato mice were genotyped using PCR to determine heterozygosity for VGAT-Cre
537 (primers 5′-3′: common, 12785—CTTCGTCATCGGCGGCATCTG; wild-type reverse 12786—
538 CAGGGCGATGTGGAATAGAAA; mutant reverse oIMR8292—CCAAAAGACGGCAATATGGT) and
539 tdtomato (primers 5′-3′: wild-type forward oIMR9020—AAGGGAGCTGCAGTGGAGTA; wild-type
540 reverse oIMR9021—CCGAAAATCTGTGGGAAGTC; mutant reverse WPRE oIMR9103—
541 GGCATTAAAGCAGCGTATCC; mutant forward tdTomato oIMR9105—
542 CTGTTCCTGTACGGCATGG). UCN3-Cre heterozygous mice (strain Tg(Ucn3-cre)KF43Gsat/
543 Mmucd, MMRRC GENSAT) were crossbred with VGAT-Flpo heterozygous mice (Jax stock
544 #007909,B6.Cg-Slc32a1 2A-Flpo-D:Het) to obtain female double heterozygous UCN3-
545 Cre::VGATFlpo mice (Slc32a1 2A-Flpo-D:Het|Ucn3-Cre:Het|Rosa26<tomato>WT); genotyped using
546 PCR for the detection of heterozygosity (primers 5′- 3′: UCN3 Forward:
547 CGAAGTCCCTCTCACACCTGGTT; Cre Reverse: CGGCAAACGGAC-AGAAGCATT; Slc32a1
548 Mutant Forward: TGC ATC GCA TTG TCT GAG TAG; Slc32a1 Mutant Reverse: GAC AGC CGT GAA
549 CAG AAG G). Female mice, aged 8 to 10 weeks, weighing between 20 g and 25 g, were individually
550 housed in ventilated cages sealed with a HEPA-filter at 25 ± 1°C in a 12:12-hour light/dark cycle, lights
551 on at 07:00 h. Vaginal smears were performed when mice are 6 weeks old between 10:00 - 12:00 h
552 daily. Only mice showing regular estrous cycles were included. All animal procedures performed were
553 approved by the King's College London Animal Welfare and Ethical Review Body. Procedures were
554 in accordance with UK Home Office regulations.

555 **Stereotaxic injection of adeno-associated virus construct and fiber-optic or mini-endoscope**
556 **GRIN lens implantation**

557 All surgical procedures were carried out under general anesthesia using ketamine (Vetalar, 100 mg/kg,
558 i.p.; Pfizer, Sandwich, UK) and xylazine (Rompun, 10 mg/kg, i.p.; Bayer, Leverkusen, Germany) under
559 aseptic conditions. Animals were secured in a David Kopf stereotaxic frame (Model 900, Kopf

560 Instruments, CA, USA). Following bilateral ovariectomy, a midline incision was made in the scalp to
561 reveal the skull. Two small bone screws were inserted into the skull. A small hole was drilled above
562 the position of the MePD. The MePD coordinate (2.29 mm lateral, 1.60 mm posterior from bregma, at
563 a depth of 5.33 mm below the skull surface) was determined according to the mouse brain atlas of
564 Paxinos and Franklin[33]. A unilateral stereotaxic viral injection was performed to target opsin or
565 fluorescent protein expression in the MePD neurons, using a robot stereotaxic system (Neurostar,
566 Tubingen, Germany), with a 5-μL Hamilton microsyringe (Esslab, Essex, UK), at the speed of 25 nl/min
567 for 10 min.

568 Two transgenic animal models were used for LH blood sampling under optogenetic stimulation:
569 UCN3Cre::VGAT-Flpo and VGAT-Cre-tdTomato. The following types of viral constructs were used in
570 separated cohorts of UCN3-Cre::VGAT-Flpo mice: (i) AAV-nEF-Con/Foff 2.0-ChRmine-oScarlet (250
571 nl, 2.1×10^{12} gc/mL, Serotype:8, #137161, Addgene, Massachusetts, USA); (ii) AAV-nEF-Con/Fon
572 2.0ChRmine-oScarlet (250 nl, 1.9×10^{12} gc/mL, Serotype:8, # 137159, Addgene, Massachusetts,
573 USA); (iii) a mixture of AAV-nEF-Con/Foff 2.0-ChRmine-oScarlet (2.1×10^{12} gc/mL, #137161) and
574 pAAV-nEF-Coff/Fon-NpHR3.3-EYFP (1.9×10^{12} gc/mL; #137159, final volume 300 nl); (iv) control virus
575 AAV-Ef1a-DIO-EYFP (250 nl, 4.4×10^{12} gc/mL, Serotype:9, #27056, Addgene, Massachusetts, USA).
576 VGATCre-tdTomato mice received unilateral injections of (i) channelrhodopsin (ChR2) viral construct,
577 (250 nl, 1.8×10^{12} gc/mL; Serotype:9; Addgene, #20298, Massachusetts, USA) or (ii) control virus,
578 AAVEf1a-DIO-EYFP (250 nl, 4.4×10^{12} gc/mL, Serotype:9; Addgene, # 27056, Massachusetts, USA)
579 into the MePD. Following injection, the needle was kept in position for 10 min before going up slowly
580 over 1 min. A unilateral fiber optic cannula (200 μm, 0.39 NA, 1.25 mm ceramic ferrule; Doric Lenses,
581 Quebec, Canada) was inserted into the right MePD 0.15 mm above the injection site. After reaching
582 the target, the fiber optic cannula was secured on the skull using dental cement (Super-Bond Universal
583 Kit, Prestige Dental, UK), bonded to the screws and skull. Finally, the incision in the scalp was closed
584 with suture. Animals were given 1 week to recover, after which they were handled 20 min daily to
585 acclimate to experimental procedures for a further 2 weeks.
586 For mini-endoscope *in vivo* calcium imaging, only UCN3-Cre::VGAT-Flpo transgenic animals were
587 used. Separate mice cohorts received the following viral injection into the MePD: (i) a mixture of pAAV-

588 Syn-Flex-rc[Chrimson-tdTomato] (2.0×10^{12} gc/mL, Serotype:5, #62723, Addgene, Massachusetts,
589 USA) + pAAV-EF1a-fDIO-GCaMP6s (2.3×10^{12} gc/mL; Serotype:8; #105715, Addgene,
590 Massachusetts, USA; final volume 400 nl); (ii) a mixture of pAAV-Syn-Flex-rc[ChrimsontdTomato]
591 (2.0×10^{12} gc/mL, Serotype:5, #62723, Addgene, Massachusetts, USA) +
592 pAAV.CAG.Flex.GCaMP6s.WPRE.SV40 (4.3×10^{12} gc/mL; Serotype:9; # 100842, Addgene,
593 Massachusetts, USA; final volume 400 nL); (iii) a mixture of control virus pAAV-hSyn-DIO-mCherry
594 (2.3×10^{12} gc/mL, Serotype:9, #50459) + pAAV-EF1a-fDIO-GCaMP6s (2.3×10^{12} gc/mL, Serotype:8,
595 #105715, final volume 400nl) . One week after administering the virus, a 600-μm diameter, 7.2-mm
596 long gradient index (GRIN) ProView™ Integrated Lens (Inscopix, PN:100-004554) was implanted at
597 the same location as the viral injection. The surface of the skull was scored, using the tip of a surgical
598 scalpel, and four screws were inserted into the skull. This was done to enhance the adhesion of dental
599 cement to the skull, thereby reducing the interference of movement on *in vivo* recording. Before
600 insertion of the GRIN lens, a 23 G needle was slowly lowered at a speed of 5.0 mm/min into the brain
601 (2.42 mm lateral, 1.52 mm posterior from bregma, depth of 5.05 mm below the skull surface) to make
602 a needle track to facilitate the insertion of the GRIN lens without causing brain distortion along its
603 route. The GRIN lens was then inserted into the brain at a rate of 0.6 mm/min, using the same
604 coordinates as the needle precutting. To secure the GRIN lens with integrated baseplate in position,
605 we used a light curing adhesive (iBond Universal, Kulzer GmbH, Leipziger, Germany) along with a
606 cured radiopaque hybrid dental cement (Gradia Direct Flo, GC corporation, Tokyo, Japan), bonding it
607 to the head screws and skull. A GRIN lens baseplate dust cover (Inscopix) was rescued in place to
608 protect the lens. After 4 weeks the mice were re-anaesthetized as described above and underwent
609 bilateral ovariectomy.

610 **Serial blood sampling for LH measurement**

611 The mouse's tail-tip was excised using a sterile scalpel. Then the chronically unilaterally implanted
612 fiber optic cannula was connected to a multimode fiber optic rotary joint patch cables (Thorlabs Ltd,
613 Ely, UK) via a ceramic mating sleeve to allow the animal freedom of movement. Mice were left for 1 h
614 to habituate. A Grass SD9B stimulator-controlled DPSS laser (Laserglow Technologies, Toronto,

615 Canada) was utilized to deliver either green light (532 nm wavelength, 10 Hz, 5 seconds on 5 seconds
616 off, 10 mW, 10-ms pulse width,) or blue light (473 nm wavelength, 5 Hz, 5 seconds on 5 seconds off,
617 5 mW, 10-ms pulse width,). The light pattern was controlled using software designed in house. After
618 1 h of acclimatization, serial blood samples (5 µL) for LH pulse measurement were collected every 5
619 min for 2 h between 10:00 - 12:00 h: 0-60 min for control blood sampling period, and 60-120 min under
620 stimulation or equivalent no-stimulation control period. Blood samples were diluted in 45 µL of
621 Phosphate-Buffered Saline (PBS) containing 0.2% Bovine Serum Albumin (BSA) and 0.05% Tween20
622 (PBST) and immediately placed on dry ice and stored at −80°C until later analysis.

623 **LH assay**

624 LH measurement was performed using an LH ELISA assay as reported previously[34]. A mouse LH
625 standard (mLH; AFP-5306A, NIDDK-NHPP, USA) was used to establish a standard curve for the
626 quantitative measurement. The following antibodies were used in the assay: (i) coating antibody
627 (RRID: AB_2665514, monoclonal antibovine LH beta subunit antiserum, 518B7, University of
628 California, CA, USA); (ii) anti-LH antibody (RRID: AB_2665533; National Hormone & Peptide
629 Program, CA, USA); (iii) secondary antibody (RRID: AB_772206, GE Healthcare, Chicago, Illinois,
630 USA). The inter-assay and intra-assay variations were 10.53% and 5.74%, respectively. The assay
631 sensitivity was 0.023 ng/mL.

632 **LH pulse statistical analysis**

633 LH pulses were verified using the Dynpeak algorithm in Scilab 5.5.2 programme[35]. The Dynpeak
634 algorithms were classified for OVX mice based on previously established parameters[36]. The average
635 LH inter-pulse interval was calculated for the 1-h control period and the 1-h stimulation period in both
636 experimental and control mice. Statistical significance was assessed using a 2-way ANOVA unless
637 otherwise stated. Data were represented as mean ± SEM and $p<0.05$ was considered significant.

638 **Mini-endoscope-based Calcium imaging**

639 **Optogenetic stimulation of MePD UCN3 neurons.** Prior to recording, animals were handled daily
640 for 5 to 6 weeks to get accustomed to the experimental setup. The Data Acquisition (DAQ) box

641 (Inscopix, PN:100-005904) was turned on and connected to the computer wirelessly. The Data
642 Acquisition Software (IDAS; Inscopix, Inc.) was accessed through the Chrome web browser on the
643 computer communicating with the DAQ box. Adequate DAQ box storage capacity was checked
644 routinely before Calcium imaging. The GRIN lens baseplate dust cover was gently removed from the
645 mouse's head, after which the minscope camera was secured to the baseplate platform. Equipped
646 with the head-mount miniscope (nVoke2, Inscopix, SN: BB-11238601), the mouse was then placed
647 back into its home cage. The optimal focal plane was chosen by adjusting the lens focus to achieve
648 clear cell morphology. The exposure time was fixed at 50 ms. The frame rate was set to 20 Hz.
649 Subsequently, gain, and LED power were optimized based on image histograms before initiating
650 recording. Two types of LED were used during the recording: (i) EX-LED (0.2-0.4 mW, 435-460 nm
651 excitation filter) for GCaMP6s signal detection in the GABA or UCN3 neurons; (ii) OG-LED (10 mW,
652 590-650 nm excitation filter) for Chrimson optogenetic stimulation of the UCN3 neurons. After the mice
653 were attached to the miniscope, they were given 1-2 h for adaptation. For stimulation of the UCN3
654 neurons, the OG-LED was set to 10 Hz, 5 sec on 5 sec off, and a 10-ms pulse width. Once the animals
655 had acclimatized, the GCaMP6s recording of the GABA neurons or UCN3 neurons was started with
656 a protocol of 2 min baseline before stimulation for 2 min. Optogenetic stimulation was randomized for
657 the 10 Hz, with a 5-min interval between each to prevent photobleaching of GCaMP6s. Once the
658 experiment was concluded, the miniscope was gently detached, and the baseplate cover was
659 reattached and secured with its screw. The recordings were performed between 9:00 h and 15:00 h.
660 Three groups of animals were included in this experiment: (i) mice with UCN3 neurons expressing
661 opsin and GABA neurons expressing GCaMP; (ii) mice with UCN3 neurons expressing both opsin
662 and GCaMP, serving as a positive control; (iii) mice with UCN3 neurons expressing mCherry and
663 GABA neurons expressing GCaMP, serving as a negative control. To quantify intra-animal variability
664 at least two independent stimulation trials were conducted with each animal, with a maximum of four
665 trials per animal.

666 **Restraint stress.** The system was set up and the mouse was connected to the miniscope as
667 described above but with the OG-LED turned off. Once the mouse had settled, the experiment started

668 with a 3 min baseline recording, followed by 3 min of recording under hand-held restraint. Finally, the
669 miniscope was detached and the baseplate cover was reattached. The experiments were performed
670 between 9:00 h and 15:00 h. The animals in this experiment were the same as those used in the
671 optogenetic stimulation protocol described above but were divided into two groups depending on
672 whether GCaMP was expressed in the UCN3 or GABA neurons, regardless of whether opsin or
673 mCherry was expressed in the UCN3 cells. A single trial per animal was performed to minimize
674 unnecessary distress, in accordance with the 3Rs principle, apart from one animal in which the
675 restraint stress experiment was performed twice to ensure this does not result in habituation.

676 ***In vivo* calcium imaging recording processing**

677 The video data, with a resolution of 1280 pixels x 800 pixels, was exported from the DAQ box through
678 the file manager to a desktop computer and processed with the Inscopix Data Processing Software
679 (IDPS). Within the IDPS, there are six essential steps for extracting single-cell calcium transient data
680 from the recorded video: down-sampling, cropping, spatial filtering, motion correction, trace
681 normalization ($\Delta F/F_0$), and cell identification. First, the video underwent both spatial down-sampling
682 and temporal down-sampling by a factor of 2 and was cropped to enhance processing speed, focusing
683 on the region of interest where the GCaMP signal was observed. Spatial filtering, with a threshold
684 ranging between 0.005 (low) and 0.5 (high) was used to distinguish individual pixels in the video
685 image, creating a high-contrast image. A mean intensity projection image was generated. Motion
686 correction was subsequently conducted, using the mean intensity projection image as a reference.
687 Motion correction was applied again using one of the frames affected by movement while
688 simultaneously drawing a region of interest (ROI) where UCN3 accumulates to enhance the
689 effectiveness of motion correction. For the recordings with GCaMP signals from GABA neurons, we
690 did not use the built-in motion correction function of IDPS. Instead, we used the MATLAB (version
691 R2022a) implementation of the open-source algorithm NoRMCorre[37] with default parameters for both
692 rigid and non-rigid (patch size 64 pixels and overlap 32) motion correction as long as a minimum
693 correlation of the frames with the mean frame above 0.8 is achieved. This was performed by doubling
694 the patch size and their overlap to 128 and 64, respectively. Corrected videos were saved in TIFF

695 format for further analysis via IDPS. Following motion correction, pixel intensity, $F(x, y)$, in each frame
696 of the movie was normalized using the following formula $\frac{(F(x,y) - F_{baseline}(x,y))}{F_{baseline}(x,y)}$, where $F_{baseline}(x, y)$ is
697 the baseline pixel intensity calculated by taking the mean value of the pixel across the entire movie.
698 Finally, regions of interest were identified automatically using the cell identification algorithm provided
699 by IDPS, based on principal component and independent component analysis (PCA-ICA algorithm).

700 **Validation of virus injection, fiber optic cannula and GRIN lens implantation**

701 Once the experimental procedures were completed, a lethal dose of ketamine was used to humanely
702 euthanize the mice. The mice were perfused transcardially with heparinized saline (5 U/ml) for 5 min,
703 followed by ice-cold 4% paraformaldehyde (PFA) for 15 min using a pump (Minipuls,156 Gilson,
704 Villiers Le Bel, France). The brains were collected and post-fixed sequentially at 4°C in a solution of
705 15% sucrose in 4% PFA and later in a solution of 30% sucrose in phosphate buffer until they sank.
706 They were then snap frozen on dry ice and stored in -80°C until processing. The brains were coronally
707 sectioned (30 μm) between +0.5 mm and -2.7 mm from the bregma using a cryostat (Bright Instrument
708 Co., Huntingdon, UK), and sections were mounted on microscope slides, air-dried, and covered with
709 slips using Prolonged Antifade mounting medium (Molecular Probes, Inc. OR, USA). The accuracy of
710 injection sites, fiber optic cannula and GRIN lens implantation were confirmed by Axioskop 2 Plus
711 microscope equipped with AXIOVISION 4.7 (Zeiss). Images were captured using Axioskop 2 Plus
712 microscope (Carl Zeiss). Only the data of mice with correct viral infection and implantation of cannula
713 and lens in the MePD were included in the analysis.

714 **Immunohistochemistry**

715 To assess the targeting of viral labeling to UCN3 neurons in the MePD, we used the indirect
716 immunofluorescence technique to localize UCN3 neurons. Every 4th section from each brain was
717 washed in potassium phosphate-buffered saline (KPBS) and incubated in blocking solution (KPBS
718 containing 1% BSA, 0.03% Triton X-100 and 5 mg/mL heparin) at room temperature for 1 hour
719 followed by incubated in a rabbit polyclonal anti-UCN3 antibody (1:2000 dilution)[38] in the blocking
720 solution (Code: PBL 7218, kindly provided by J. Vaughan, Salk Institute, La Jolla, CA, USA) for 48
721 hours at 4°C. The brain sections were then processed with goat anti-rabbit IgG (H + L), a biotinylated

722 secondary antibody (1:1000 dilution; Cat. No. BA-1000, Vector Laboratories, Burlingame, CA, USA)
723 overnight at 4°C. After rinses in KPBS, visualization of UCN3 immunoactivity was achieved using
724 Streptavidin, Alexa Fluor 405 conjugate (1:200 dilution; Cat. No. S 32351, Thermo Fisher Scientific,
725 Waltham, MA, USA) for 2 hours at room temperature. The sections were finally washed, mounted
726 onto slides and cover slipped. Omission of the UCN primary antibody and its pre-incubation resulted
727 in the absence of specific staining. Brain sections from each experimental group were processed on
728 the same day to control for inter-batch variability. To preserve the fluorescence of the virally expressed
729 proteins, all subsequent steps were performed in a dark box. Semiquantitative analysis of
730 immunostaining data was carried out on AxioVision microscope image system. UCN3-positive
731 neurons were identified by Alexa Fluor 405 fluorescence, while native fluorescence (e.g. tdTomato or
732 oScarlet) was used for virus-transduced neurons identification. The number of virus-labeled, UCN3-
733 immunoreactive cells and co-localized cells in the MePD were quantified on 4 sections from each
734 mouse brain. Targeting efficiency was defined as the percentage of virus-labeled cells that were also
735 positive for UCN3.

736 **Data analysis**

737 The data processing protocol we employ in this study was performed in two phases: pre-intervention
738 and intervention (either via optogenetic stimulation or restraint stress). For our analysis, we use the
739 smoothed deconvolved traces generated by the OASIS method[39], which improves the signal-to-noise
740 ratio (SNR) and mitigates noise interference. All traces are rescaled between 0 and 1 (min-max
741 normalization), and then further normalized to mean zero and unit variance. The analysis process is
742 divided into three key steps: i) identification of GABA cells co-expressing UCN3 and removing them
743 from further analysis; ii) estimating and comparing functional connectivity before and during
744 intervention; iii) clustering analysis based on pairwise association-derived dissimilarity scores. In step
745 (i), we use power spectral density (PSD) analysis and K-means clustering (using Euclidean distance)
746 to identify GABA neurons with activity that mimics the pattern of optic stimulation, evidence that they
747 are co-expressing UCN3.

748 **PSD filtering.** For each trace, we compute the PSD during the stimulation phase. Cells with PSD
749 values at 0.1 Hz (the frequency of the stimulus 5 sec and 5 sec off cycle) above 0.37 Hz^{-1} are labelled
750 as co-expressing UCN3. This threshold is determined from recordings of UCN3 cells under optic
751 stimulation, by calculating the median of the minimum PSD values at 0.1 Hz from each dataset (see
752 Supplementary Fig. 2**B**).

753 **K-means clustering.** Using the Euclidean distance metric, we cluster the traces during the stimulation
754 phase into two groups, aiming to separate neurons into GABA-only neurons and neurons co-
755 expressing UCN3 and GABA. Clustering separated a small group of neurons with activity mimicking
756 the optic stimulation oscillatory pattern (see Supplementary Fig. 2**C**). Recordings of MePD UCN3
757 neurons shows that under optogenetic stimulation their activity rises and declines in phase with on
758 and off periods of stimulation (shown in Fig. 3**A**); therefore, this small number of cells was labeled as
759 co-expressing UCN3.

760 The union of neurons identified by either method as co-expressing UCN3 and GABA are excluded
761 from further analysis. By applying both filters, we aim to robustly identify purely GABA-expressing
762 neurons. We acknowledge the possibility that some cells may pass through the filters or that a few
763 purely GABA-expressing neurons may be inadvertently excluded. However, our dual approach of
764 employing PSD analysis and K-means clustering minimizes this possibility and is essential to ensure
765 our analysis remains focused exclusively on GABA-expressing neurons. Nevertheless, we take a
766 further step and visually inspect the calcium recording traces for any potential anomalies such as
767 regular oscillations in-phase with the stimulation and/or massive increase in calcium level during the
768 intervention period. Any identified anomalies of this sort are also dropped from datasets.

769 **Comparing pre-intervention and intervention cell-cell interaction strength**

770 Following step (i), the remaining dataset contains only traces associated with GABA neurons, which
771 are not directly activated by our optic stimulation protocol. In step (ii), we assess the functional
772 connectivity between the observed neurons using Pearson's correlation[40] defined as

773 $$corr(x,y) = \frac{R(x,y)}{\sqrt{R(x,x)R(y,y)}},$$

where $R(x,y) = \sum_{i=1}^{N}(x_i - \bar{x})(y_i - \bar{y})$ represents cross-correlation with N as the length of x and y. Using the above measures, we construct the corresponding cross-correlation matrices (see for an example Fig. 1**H&I**).

To evaluate changes in pairwise cell interactions between the pre-intervention and intervention phases, we compute the pairwise Riemannian distance[41] between correlation matrices from pre-intervention and intervention episodes. The Riemannian distance here is defined as

$$d(A,B) = \left(\sum_i \ln(\lambda_i)^2\right)^{1/2},$$

where ln is the natural logarithm and $\lambda_.$ indicates the joint eigenvalues of symmetric positive definite (SPD) cross-correlation matrices A and B. The size of the matrices directly affects the Riemannian distance, therefore, we normalize each Riemannian distance by the average Riemannian distance computed from 100 pairs of randomly generated SPD matrices of the same size. To make sure that random generation is uniform in the space of SPD matrices, we employ the Metropolis-Hasting method introduced in[42]. Normalizing the Riemannian distances guarantees that the distance is not influenced by matrix size. To assess the effect of experimental conditions on Riemannian distances while accounting for the hierarchical structure of the data, we employed a linear mixed-effects model[43]. Specifically, we modeled repeated measurements nested within individual animals, as follows:

$$\mathrm{y} \sim \mathrm{condition} + (1 \mid \mathrm{Animal}) + (1 \mid \mathrm{Animal{:}\,Repeat}),$$

where y denotes the computed Riemannian distance, while condition represents whether the experiment was control, stimulation or restraint stress. The model was fitted using maximum likelihood estimation.

Clustering analysis

In step (iii), we apply agglomerative hierarchical clustering (using the average linkage criterion; package in scikit-learn Python™) to classify cells based on the dissimilarity of their calcium activity, given as

$$D(x, y) = 1 - corr(x, y).$$

To determine the optimal number of clusters and robustness of clustering, we employed a bootstrapping technique. This involved resampling (without replacement) 75% of the cells and clustering the resulting dataset with different numbers of clusters (2, 3, and 4) using hierarchical or K-means clustering with either the covariance or correlation as the dissimilarity measure. This resampling process was repeated 100 times.

For each resample dataset, we evaluate the clustering performance, using the Silhouette Coefficient (SC)[42] which measures the cohesion within clusters and their separation, with values ranging from -1 (poor performance) to 1 (good performance). Results of the evaluation are given in Supplementary Figs. 4-6, showing that the SC is significantly higher for 2 clusters compared to 3 or 4 clusters in the case of both hierarchical and K-means clustering.

Modeling

We build on our previously published modeling framework of MePD circuit[11] by incorporating dynamic stimulation by UCN3 neurons as observed experimentally (as shown in Fig. 3). To this end we define input from UCN3 neurons into the populations of glutamatergic neurons and GABA interneurons with a strength given by the parameter γ. The activity of UCN3 neurons during stimulation is approximated via sinusoidal function:

$$U_{stim}(t) = \gamma B + Asin(2\pi f t),$$

where the parameter f is the frequency of the wave. Parameter B represents the constant excitatory drive, potentially mediated by slow neuropeptide action, while the term $Asin(2\pi f t)$ describes faster neurotransmitter-driven-driven input aligned with optogenetic stimulation frequency. We approximate UCN3 neuron activity during restraint stress using two exponential functions:

$$U_{stress}(t) = \gamma\big(at\exp(-r_2 t) + b(1 - \exp(-r_1 t))\big),$$

821 where the function initially increases with magnitude a then decreases to a plateau value
822 given by the parameter b. The parameters r_2 and r_1 are responsible for the rate of increase
823 of the first term and rate of decrease to a plateau in the second term.

824 Briefly, the model captures the dynamics of the MePD intracellular calcium activity of three
825 populations: glutamatergic neuronal population (excitatory) and the populations of GABA interneurons
826 and GABA efferent neurons (inhibitory). We build on our previous work[11] by assuming that excitatory
827 (UCN3) input is provided to the populations of GABA interneurons and glutamate (Fig 3). Previous
828 analysis of the model indicated that negative feedback between GABA and glutamatergic neuronal
829 populations as well as glutamatergic self-excitation are critical mechanisms for inducing oscillatory
830 dynamics[11]. However, providing glutamatergic inputs to both populations of GABA neurons results in
831 a null phase difference between the populations. Therefore, we opted to provide glutamatergic input
832 only to the population of GABA efferent neurons.

833 To investigate how the amygdala modulates the activity in the GnRH pulse generator, we couple the
834 above-described MePD model to our KNDy network model, where the oscillatory dynamics of the
835 KNDy acts as a proxy of LH pulsatility[26]. Here we couple the model via providing only inhibitory output
836 from MePD GABA efferent neurons population to KNDy, as it was previously shown that glutamate
837 plays a modulatory role to the MePD output rather than directly affecting the KNDy network[11]. We then
838 calibrate the coupled model by reproducing the experimental results from Ivanova et al.[23]
839 (Supplementary Fig. 8). Further modeling details, such as equations governing model dynamics and
840 model parameter values, can be found in Supplementary Information. The simulations have been
841 done in MATLAB (version R2023b).

842 Data Availability

843 Source data are provided with this paper. Further information that supports the findings of this study
844 is available from the corresponding authors upon request.

845 ## Code Availability

846 The code for reproducing the data analysis (Python™), mathematical modeling (MATLAB), and figure
847 generation for both the main text and Supplementary information, along with the datasets used in the
848 analysis, is publicly available at: https://github.com/mv-kr/MePD_GABA.

849 ## References

850 1. Yeo, S.-H., Kyle, V., Blouet, C., Jones, S. & Colledge, W. H. Mapping neuronal inputs to Kiss1
851 neurons in the arcuate nucleus of the mouse. *PLOS ONE* **14**, e0213927 (2019).
852 2. Moore, A. M., Coolen, L. M. & Lehman, M. N. Kisspeptin/Neurokinin B/Dynorphin (KNDy) cells as
853 integrators of diverse internal and external cues: evidence from viral-based monosynaptic tract-
854 tracing in mice. *Sci. Rep.* **9**, 14768 (2019).
855 3. Li, X. F. & O'Byrne, K. T. Stress and the Reproductive System. in *Knobil and Neill's Physiology of*
856 *Reproduction: Two-Volume Set* vol. 2 1637–1660 (ELSEVIER SCIENCE INC, 2014).
857 4. Yu, J., Li, X.-F., Tsaneva-Atanasova, K., Zavala, E. & O'Byrne, K. T. Chemogenetic activation of
858 PVN CRH neurons disrupts the estrous cycle and LH dynamics in female mice. *Front. Endocrinol.*
859 **14**, 1322662 (2023).
860 5. Kreisman, M. J., Tadrousse, K. S., McCosh, R. B. & Breen, K. M. Neuroendocrine Basis for
861 Disrupted Ovarian Cyclicity in Female Mice During Chronic Undernutrition. *Endocrinology* **162**,
862 bqab103 (2021).
863 6. Bethea, C. L., Centeno, M. L. & Cameron, J. L. Neurobiology of Stress-Induced Reproductive
864 Dysfunction in Female Macaques. *Mol. Neurobiol.* **38**, 199–230 (2008).
865 7. Herod, S. M., Pohl, C. R. & Cameron, J. L. Treatment with a CRH-R1 antagonist prevents stress-
866 induced suppression of the central neural drive to the reproductive axis in female macaques. *Am.*
867 *J. Physiol. Endocrinol. Metab.* **300**, E19-27 (2011).
868 8. Nair, B. B. *et al.* Impact of chronic variable stress on neuroendocrine hypothalamus and pituitary
869 in male and female C57BL/6J mice. *J. Neuroendocrinol.* **33**, e12972 (2021).
870 9. Comninos, A. N. *et al.* Kisspeptin signaling in the amygdala modulates reproductive hormone
871 secretion. *Brain Struct. Funct.* **221**, 2035–2047 (2016).

872 10. Lass, G. *et al.* Optogenetic stimulation of kisspeptin neurones within the posterodorsal medial
873 amygdala increases luteinising hormone pulse frequency in female mice. *J. Neuroendocrinol.* **32**,
874 e12823 (2020).
875 11. Nechyporenko, K. *et al.* Neuronal network dynamics in the posterodorsal amygdala: shaping
876 reproductive hormone pulsatility. *J. R. Soc. Interface* **21**, 20240143 (2024).
877 12. Adekunbi, D. A. *et al.* Role of amygdala kisspeptin in pubertal timing in female rats. *PLoS ONE*
878 **12**, e0183596 (2017).
879 13. Ivanova, D. *et al.* Role of Posterodorsal Medial Amygdala Urocortin-3 in Pubertal Timing in Female
880 Mice. *Front. Endocrinol.* **13**, (2022).
881 14. Adekunbi, D. A. *et al.* Kisspeptin neurones in the posterodorsal medial amygdala modulate sexual
882 partner preference and anxiety in male mice. *J. Neuroendocrinol.* **30**, e12572 (2018).
883 15. Wu, Y. E. *et al.* Neural control of affiliative touch in prosocial interaction. *Nature* **599**, 262–267
884 (2021).
885 16. Ivanova, D. *et al.* Urocortin3 in the Posterodorsal Medial Amygdala Mediates Stress-induced
886 Suppression of LH Pulsatility in Female Mice. *Endocrinology* **162**, 1–14 (2021).
887 17. McIntyre, C. *et al.* GABA Signaling in the Posterodorsal Medial Amygdala Mediates Stress-
888 induced Suppression of LH Pulsatility in Female Mice. *Endocrinology* **164**, 1–11 (2023).
889 18. Keshavarzi, S., Sullivan, R. K. P., Ianno, D. J. & Sah, P. Functional Properties and Projections of
890 Neurons in the Medial Amygdala. *J. Neurosci.* **34**, 8699–8715 (2014).
891 19. Choi, G. B. *et al.* Lhx6 delineates a pathway mediating innate reproductive behaviors from the
892 amygdala to the hypothalamus. *Neuron* **46**, 647–660 (2005).
893 20. Bian, X. Physiological and morphological characterization of GABAergic neurons in the medial
894 amygdala. *Brain Res.* **1509**, 8–19 (2013).
895 21. Lewis, K. *et al.* Identification of urocortin III, an additional member of the corticotropin-releasing
896 factor (CRF) family with high affinity for the CRF2 receptor. *Proc. Natl. Acad. Sci. U. S. A.* **98**,
897 7570–7575 (2001).
898 22. Shemesh, Y. *et al.* Ucn3 and CRF-R2 in the medial amygdala regulate complex social dynamics.
899 *Nat. Neurosci.* **19**, 1489–1496 (2016).

900 23. Ivanova, D., Li, X.-F., McIntyre, C. & O'Byrne, K. T. Posterodorsal Medial Amygdala Urocortin-3,
901 GABA, and Glutamate Mediate Suppression of LH Pulsatility in Female Mice. *Endocrinology* **164**,
902 1–13 (2023).
903 24. Yuste, R., Cossart, R. & Yaksi, E. Neuronal ensembles: Building blocks of neural circuits. *Neuron*
904 **112**, 875–892 (2024).
905 25. Arrigoni, E. & Saper, C. B. What optogenetic stimulation is telling us (and failing to tell us) about
906 fast neurotransmitters and neuromodulators in brain circuits for wake-sleep regulation. *Curr. Opin.*
907 *Neurobiol.* **29**, 165–171 (2014).
908 26. Voliotis, M. *et al.* The Origin of GnRH Pulse Generation: An Integrative Mathematical-Experimental
909 Approach. *J. Neurosci.* **39**, 9738–9747 (2019).
910 27. Hochgerner, H. *et al.* Neuronal types in the mouse amygdala and their transcriptional response to
911 fear conditioning. *Nat. Neurosci.* **26**, 2237–2249 (2023).
912 28. Li, Y. *et al.* Neuronal Representation of Social Information in the Medial Amygdala of Awake
913 Behaving Mice. *Cell* **171**, 1176-1190.e17 (2017).
914 29. Pardo-Bellver, C., Cádiz-Moretti, B., Novejarque, A., Martínez-García, F. & Lanuza, E. Differential
915 efferent projections of the anterior, posteroventral, and posterodorsal subdivisions of the medial
916 amygdala in mice. *Front. Neuroanat.* **6**, 33 (2012).
917 30. Polepalli, J. S., Gooch, H. & Sah, P. Diversity of interneurons in the lateral and basal amygdala.
918 *Npj Sci. Learn.* **5**, 10 (2020).
919 31. Patel, A. H. *et al.* Kisspeptin in functional hypothalamic amenorrhea: Pathophysiology and
920 therapeutic potential. *Ann. N. Y. Acad. Sci.* **1540**, 21–46 (2024).
921 32. Barbagallo, F. *et al.* Gene-environment interaction in functional hypothalamic amenorrhea. *Front.*
922 *Endocrinol.* **15**, 1423898 (2024).
923 33. Paxinos, G. & Franklin, K. B. J. *Paxinos and Franklin's the Mouse Brain in Stereotaxic*
924 *Coordinates*. (2019).
925 34. Steyn, F. J. *et al.* Development of a Methodology for and Assessment of Pulsatile Luteinizing
926 Hormone Secretion in Juvenile and Adult Male Mice. *Endocrinology* **154**, 4939–4945 (2013).

35. Vidal, A., Zhang, Q., Médigue, C., Fabre, S. & Clément, F. DynPeak: An Algorithm for Pulse Detection and Frequency Analysis in Hormonal Time Series. *PLOS ONE* **7**, e39001 (2012).
36. Yang, J. A. *et al.* Acute Psychosocial Stress Inhibits LH Pulsatility and Kiss1 Neuronal Activation in Female Mice. *Endocrinology* **158**, 3716–3723 (2017).
37. Pnevmatikakis, E. A. & Giovannucci, A. NoRMCorre: An online algorithm for piecewise rigid motion correction of calcium imaging data. *J. Neurosci. Methods* **291**, 83–94 (2017).
38. Battagello, D. S. *et al.* Anatomical Organization of Urocortin 3-Synthesizing Neurons and Immunoreactive Terminals in the Central Nervous System of Non-Human Primates [Sapajus spp.]. *Front. Neuroanat.* **11**, (2017).
39. Friedrich, J., Zhou, P. & Paninski, L. Fast online deconvolution of calcium imaging data. *PLOS Comput. Biol.* **13**, (2017).
40. Rice, J. A. *Mathematical Statistics and Data Analysis*. (Thomson/Brooks/Cole, Belmont, CA, 2007).
41. Moakher, M. A Differential Geometric Approach to the Geometric Mean of Symmetric Positive-Definite Matrices. *SIAM J. Matrix Anal. Appl.* **26**, 735–747 (2005).
42. Córdoba, I., Varando, G., Bielza, C. & Larrañaga, P. A Fast Metropolis-Hastings Method for Generating Random Correlation Matrices. in *Intelligent Data Engineering and Automated Learning – IDEAL 2018* (eds. Yin, H., Camacho, D., Novais, P. & Tallón-Ballesteros, A. J.) 117–124 (Springer International Publishing, Cham, 2018). doi:10.1007/978-3-030-03493-1_13.
43. Harrison, X. A. *et al.* A brief introduction to mixed effects modelling and multi-model inference in ecology. *PeerJ* **6**, e4794 (2018).

Acknowledgements

We thank Ms Sumi Mathew for her technical support with genotyping mice.

S.F., M.V., K.T.A., K.T.O., X.F.L. gratefully acknowledge the financial support of BBSRC via grants BB/W005913/1 (KCL), BB/W005883/1 (Exeter) and BB/S019979/1. KTA gratefully acknowledges the financial support of the EPSRC via grant EP/T017856/.

Contributions

J.Y. contributed data acquisition and data analysis, S.F. contributed data analysis, K.N. contributed modeling, M.V. contributed managing data analysis, X.F.L. contributed managing data acquisition and analysis, H.Y. contributed data acquisition, Y.L. contributed data acquisition, J.Y. contributed data acquisition, O.H. contributed data acquisition, R.D.B. contributed data acquisition, B.S. contributed data acquisition, K.T.O., K.T.A., X.F.L. and M.V. contributed to managing the project. All authors contributed to writing the manuscript.

Competing interests

The authors declare no competing interests.

Corresponding author

Correspondence and requests for materials should be addressed to Krasimira Tsaneva-Atanasova (K.Tsaneva-Atanasova@exeter.ac.uk), Kevin T. O'Byrne (kevin.o'byrne@kcl.ac.uk), Margaritis Voliotis (m.voliotis@exeter.ac.uk).

Open Access

For the purpose of open access, the authors have applied a 'Creative Commons Attribution (CC BY) licence to any Author Accepted Manuscript version arising from this submission.